Journal of Materials Chemistry A

ROYAL SOCIETY OF CHEMISTRY

REVIEW

View Article Online
View Journal | View Issue

Cite this: J. Mater. Chem. A, 2025, 13, 6152

Materials with the barocaloric effect for solid-state refrigeration

Ying Sun,†[a] Shihai An,†[a] Yihong Gao,[cde] Zibing Yu,[cde] Xiuliang Yuan,[a] Zhijie Ma,[a] Kewen Shi,[b] Fengxia Hu *[cde] and Cong Wang *[b]

As a low-carbon and energy-efficient refrigeration approach, barocaloric refrigeration is considered a promising alternative to traditional vapor compression refrigeration. However, finding excellent barocaloric materials remains a significant challenge, as they require low driving pressures, large isothermal entropy changes, and wide refrigeration temperature ranges. In this review, barocaloric materials are classified into four categories, with their respective barocaloric parameters calculated and analyzed. It is observed that different types of barocaloric materials exhibit unique distribution patterns based on their numerical values. By combining the analysis of the microstructure and the dynamics during phase transitions, the driving pressure and isothermal entropy change are considered to be related to the internal force resisting pressure and the changes in atomic degrees of freedom during the phase transition, respectively. This review offers new insights into the mechanisms of barocaloric effects and material selection. Finally, potential avenues for future development in this field are discussed.

Received 17th October 2024
Accepted 2nd January 2025

DOI: 10.1039/d4ta07404a

rsc.li/materials-a

1 Introduction

In the contemporary world, refrigeration accounts for nearly 25% of the total electricity consumption and plays a critical role in various fields, such as food preservation, industrial production and medical care.[1,2] Nevertheless, the conventional vapor compression refrigeration system poses a significant environmental risk due to greenhouse gas emissions, necessitating an alternative refrigeration technology to replace it.[3,4] Solid-state refrigeration has emerged as an environmentally sustainable refrigeration technology with the potential to supplant conventional vapor compression systems.[5,6] Based on the caloric effects resulting from external fields, solid-state refrigeration can be broadly categorized into three types: the magnetocaloric effect,[7,8]

[a]School of Physics, Beihang University, Beijing 100191, China
[b]School of Integrated Circuit Science and Engineering, Beihang University, Beijing 100191, China. E-mail: congwang@buaa.edu.cn
[c]Beijing National Laboratory for Condensed Matter Physics, Institute of Physics, School of Physical Sciences, Beijing 100190, P. R. China. E-mail: fxhu@iphy.ac.cn
[d]Songshan Lake Materials Laboratory, Dongguan, Guangdong 523808, P. R. China
[e]Chinese Academy of Sciences, University of Chinese Academy of Sciences, Beijing 101408, P. R. China
† These authors contributed equally to this work.

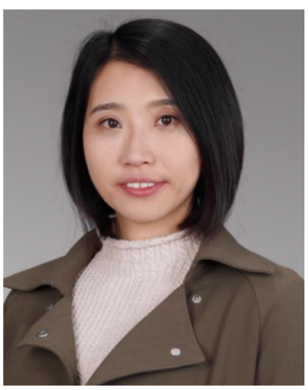

Ying Sun

Ying Sun is a Professor at the School of Physics, Beihang University. She earned her PhD in condensed matter physics from Beihang University in 2010. Her research focuses on the physical properties of strongly correlated systems under external fields such as pressure, magnetic fields, and temperature. Her current interest is in exploring new material systems with barocaloric effects.

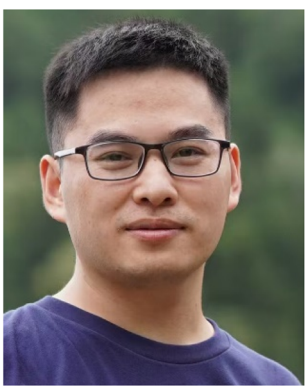

Shihai An

Shihai An is a PhD student at the School of Physics at Beihang University. He graduated with a Master's degree from the same institution. His research interests focus on the barocaloric and multicaloric effects of intermetallic compounds. His current interests also include the development of physical property measurement techniques under uniaxial stress and hydrostatic pressure.

induced by a magnetic field; electrocaloric effect,[9,10] induced by an electric field; and mechanocaloric effect,[11,12] which includes the elastocaloric effect[13,14] induced by uniaxial stress and the barocaloric effect (BCE)[15,16] induced by hydrostatic pressure. The magnetocaloric and electrocaloric effects have been extensively researched and yielded remarkable results over the past few decades. Recently, the barocaloric effect has attracted increasing research attention due to its readily available inducing fields and high energy efficiency.[17,18]

The barocaloric effect refers to the phenomenon where the application of hydrostatic pressure to a material induces a caloric effect.[19] Generally, it is characterized by isothermal entropy changes and adiabatic temperature changes.[15] Depending on the endothermic and exothermic processes during pressure application, the BCE can be classified into two types: the conventional BCE and inverse BCE. In the conventional BCE, the material undergoes exothermic processes when hydrostatic pressure is applied and endothermic processes upon its release, whereas in the inverse BCE, the material undergoes endothermic processes when hydrostatic pressure is applied and exothermic processes upon its release.[20] Based on the magnitude of the isothermal entropy change, the BCE is commonly classified into two categories: the giant and colossal BCE. The former exhibits an isothermal entropy change an order of magnitude greater than 1 J kg^{-1} K^{-1}, while the latter displays an entropy change two orders of magnitude greater than 1 J kg^{-1} K^{-1}.[21]

In 1998, K. Alex Müller *et al.* introduced the concept of adiabatic pressure-induced cooling, and investigated the caloric effect resulting from the pressure-induced transition of Pr^{3+} ions from the singlet state to the doublet state in $Pr_{1-x}La_xNiO_3$, for ultra-low temperature refrigeration applications.[22] Subsequently, Strassle *et al.* coined the term 'barocaloric effect' for the pressure-induced caloric phenomenon and investigated the extremely low temperature cooling effect in rare earth materials such as CeSb,[23,24] HoAs,[25] $Ce_3Pd_{20}Ge_6$,[26] *etc.* Initially, the reported BCE mainly focused on the low-temperature range, aiming to achieve temperatures approaching the liquid helium range through the application of the BCE.[22] In recent decades, research has extended to room-temperature applications of the BCE, since Manosa *et al.* first reported the near-room temperature giant BCE in the shape memory alloy Ni–Mn–In.[15] To date, numerous significant advancements have been documented. Barocaloric materials exhibit not only a large entropy change and refrigeration efficiencies, but also minimal driving pressures akin to those in traditional vapor compression refrigeration systems. For instance, the plastic crystal NPG demonstrates an isothermal entropy change ($|\Delta S_{it}| \approx 389$ J kg^{-1} K^{-1}) more than ten times that of typical caloric effect materials (including magnetocaloric, electrocaloric, and elastocaloric).[16] In the hybrid perovskite $[TPrA][Mn(dca)_3]$, a fully reversible isothermal entropy change can be achieved with an applied pressure of only 70 bar, which is comparable to the pressure required for traditional refrigeration (approximately 20 bar).[5] Nevertheless, the practical application of barocaloric materials remains a challenge, as the pressure field by the BCE and cooling temperature range required are difficult to apply in typical room temperature refrigeration scenarios. In addition, significant potential exists in exploring new barocaloric materials which can be used for the BCE in cryogenic cooling. Due to the limited research on cryogenic cooling in barocaloric materials, this article focuses on the analysis of room temperature barocaloric materials.[27]

From the current research on the BCE, obtaining the largest isothermal entropy change and the widest refrigeration temperature range with the smallest possible pressure remains a significant challenge. Based on this challenge, we summarized and discussed the reported barocaloric materials and explored the relationship between barocaloric parameters and material properties to promote the application of barocaloric refrigeration. In this review, we categorize barocaloric materials into four categories based on their chemical bond characteristics and elemental composition: intermetallic compounds, ionic compounds, organic–inorganic hybrid materials, and organic compounds (Fig. 1). We then summarize and calculate the BCE based on various performance indicators, including the isothermal entropy change (ΔS_{it}), adiabatic temperature change (ΔT_{ad}), pressure sensitivity (dT/dp), refrigeration capacity (RC), minimum reversible pressure (p_{min}^{rev})and refrigeration temperature range (T_{span}).

Fengxia Hu

Fengxia Hu, a Professor at the Institute of Physics, Chinese Academy of Sciences, since 2008, received her PhD in condensed matter physics in 2002. She has long been committed to the study of magnetocaloric, barocaloric, and multicaloric effects, as well as the solid-state refrigeration applications of various materials. Her current interests also include oxide spintronics, interface orbital reconstruction, and spin regulation.

Cong Wang

Cong Wang, a Professor at the School of Integrated Circuit Science and Engineering, Beihang University, received his PhD in 1995 from the Institute of Physics, Chinese Academy of Sciences. His research focuses on structure, and magnetic and caloric properties of intermetallic compounds, including baromagnetic and barocaloric effects, negative/zero thermal expansion and the anomalous Hall effect.

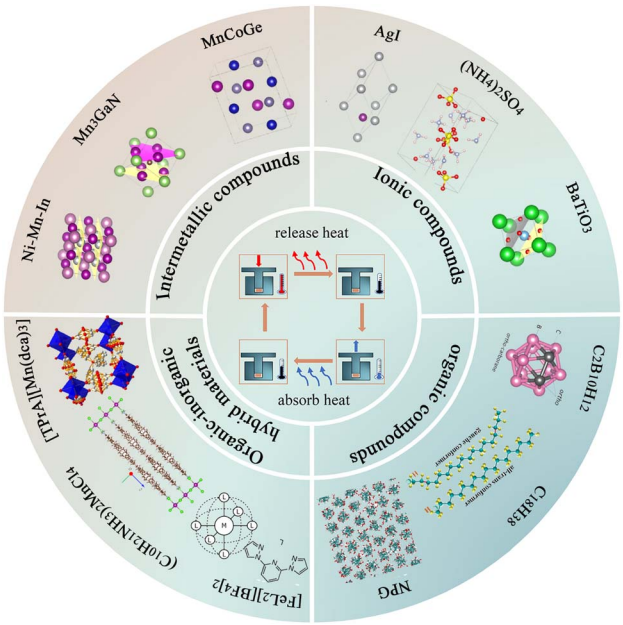

Fig. 1 Categorization schematic of barocaloric materials, which divides giant or colossal BCE materials into four categories. A schematic of the barocaloric refrigeration cycle is depicted in the center of the figure. The diagram includes a selection of representative materials for each category, for example, Ni–Mn–In, Mn_3GaC, MnCoGe, AgI, $(NH_4)_2SO_4$, $BaTiO_3$, $C_2B_{10}H_{12}$, ($C_{18}H_{38}$, (reproduced from ref. 29 with permission from Springer Nature, copyright 2022), NPG, (reproduced from ref. 16 with permission from Springer Nature, copyright 2019.), $[FeL_2][BF_4]_2$, (reproduced from ref. 30 with permission from John Wiley and Sons, copyright 2019.), $(C_{10}H_{21}NH_3)_2MnCl_4$, (reproduced from ref. 31 with permission from John Wiley and Sons, copyright 2021), and [TPrA][Mn(dca)$_3$]. (Reproduced from ref. 5 with permission from Springer Nature, copyright 2017.)

2 Barocaloric materials

2.1 Intermetallic compounds

Compounds consisting of metals, occasionally incorporating trace amounts of non-metal elements, that are predominantly bonded with metal bonds are termed intermetallic compounds. Intermetallic compounds exhibit giant barocaloric effects, such as Ni–Mn–In,[15] Ni–Mn–Ti,[36] MnCoGe,[47] MnNiGe,[49] Mn_3GaN[51] and Mn_3NiN.[52] Based on their atomic composition, intermetallic compounds are divided into several families, such as Ni_2MnZ,[55–57] MM′X,[47,49] and M_3XA.[51,52] In intermetallic compounds, some materials exhibit the conventional BCE while others exhibit the inverse BCE.

The type of BCE that occurs in a material is related to the volume which either shrinks or expands during the phase transition. This can be seen in the Clausius–Clapeyron relation.[51]

$$\frac{dT}{dp} = \frac{V\Delta\omega}{\Delta S} \quad (1)$$

Here ΔS is the entropy of the phase transition, where $\Delta\omega$ is the volume difference (in%) between the high temperature phase and the low temperature phase. dT/dp is the rate of change of the phase transition temperature with pressure (per unit pressure). dT/dp is the sensitivity of the phase transition temperature to pressure. If we consider the sign of the variable, a positive dT/dp corresponds to the conventional BCE, while a negative value indicates the inverse BCE. Due to the energy required to induce the transformation of the low-temperature phase into the high-temperature phase, the total phase transition entropy change ΔS is always positive in the heating process. From the above Clausius–Clapeyron relation, the sign of $\Delta\omega$ determines the sign of dT/dp. So, the phase transition with positive thermal expansion is accompanied by a conventional BCE, and the phase transition with negative thermal expansion is an inverse BCE. This aligns with the results from experimental observations (Tables 1 and 2). Certainly, this also applies to the criterion of the BCE type (conventional or inverse BCE) of other barocaloric materials.

2.1.1 Ni_2MnZ. The room temperature giant BCE is reported for the first time in the magnetic shape memory alloy $Ni_{49.26}Mn_{36.08}In_{14.66}$,[15] which is a member of the Ni_2MnZ (Z = Ga, In, Sn, Sb, *etc.*) family. As pressure increases, the phase transition temperature shifts toward higher temperatures. The conventional BCE occurs in $Ni_{49.26}Mn_{36.08}In_{14.66}$. The high-temperature Heusler phase transformed into the low-temperature martensite phase during the transformation process. The martensitic transformation is accompanied by a volume expansion ($\Delta\omega \approx 0.4\%$), and this phase transition is sensitive to pressure ($dT/dp \approx 1.8$ K kbar^{-1}). Applying a hydrostatic pressure of $p \approx 2.6$ kbar can generate the entire phase transition entropy ($|\Delta S_{it}| \approx 24.4$ J kg^{-1} K^{-1}). Meanwhile the phase transition behavior in the Ni–Mn–In system is sensitive to composition.[32] By regulating the composition of Ni–Mn–In, the relative distance between the Curie and martensitic transformation temperatures can be adjusted. Experimental results demonstrate that the BCE is most pronounced when the martensite transformation temperature is adjusted to be above the Curie transformation temperature. When the martensite transformation temperature is lower than the Curie transformation temperature, all BCE indicators begin to decline. Furthermore, adjusting the composition can effectively reduce thermal hysteresis, obtaining alloys with low thermal hysteresis.

Another Ni_2MnZ alloy that exhibits giant BCE properties is the Ni_2MnTi system.[94] Doping the alloy with a small amount of B atoms yields $(Ni_{50}Mn_{31.5}Ti_{18.5})_{99.8}B_{0.2}$.[36] On applying a pressure of approximately 4 kbar to $(Ni_{50}Mn_{31.5}Ti_{18.5})_{99.8}B_{0.2}$, an entropy change associated with the phase transition of $|\Delta S_{it}| \approx 35$ J kg^{-1} K^{-1} can be generated. In this alloy, the contribution of magnetic entropy to the total entropy is negligible due to the lack of ferromagnetic order in both the martensite and austenite phases. The giant BCE is primarily attributed to the change in volume entropy. In the Ni_2MnTi system, $Ni_{35.5}Co_{14.5}Mn_{35}Ti_{15}$ can be obtained by partially replacing Ni atoms with Co atoms. $Ni_{35.5}Co_{14.5}Mn_{35}Ti_{15}$ undergoes a martensitic transformation accompanied by a change in magnetization, and its giant BCE arises from its volume and magnetization discontinuity.[37] Compared to $(Ni_{50}Mn_{31.5}Ti_{18.5})_{99.8}B_{0.2}$, this alloy sacrifices a large entropy change ($|\Delta S_{it}|$ from 35 J kg^{-1} K^{-1} to

Table 1 Physical parameters of intermetallic compounds exhibiting a giant barocaloric effect[a]

Materials	T [K]	p [kbar]	$\lvert\Delta S_{it}\rvert$ [J kg^{-1} K^{-1}]	$\Delta\omega$ [%]	$\lvert\Delta T_{ad}\rvert$ [K]	$(dT/dp)_h$ [K kbar^{-1}]	$(dT/dp)_c$ [K kbar^{-1}]	ΔT_{hys} [K]	ΔT^{p}_{hys} [K]	ΔT_{width} [K]	ΔT^{p}_{width} [K]	RC [J kg^{-1}]	Ref.
$Ni_{49.26}Mn_{36.08}In_{14.66}$	300	2.6	24.4	0.4	4.5	—	1.8	4.4	—	6.7	5.8	104	15
$Ni_{2.05}Mn_{1.30}In_{0.65}$	336	2.6	26.8*	—	3.1(d)	0.9	1.6	10.4	8.4	10	10	165	32
$Ni_{44.6}Co_{5.5}Mn_{35.5}In_{14.4}$	284	5.9	14.3	0.54	6	5.1	4.7	19.3	18.7	6.3	6.4	399	33
$Ni_{42.47}Co_{8.87}Mn_{31.67}Ga_{14.98}In_{2.01}$	424	2.7	14.5	0.7	—	2.1	3.2	15	10	20	17	215	34
$Ni_{58.3}Mn_{17.1}Ga_{24.6}$	322	10.5	13.6	—	2.8	—	0.4	9.8	—	7.2	—	56	35
$(Ni_{50}Mn_{31.5}Ti_{18.5})_{99.8}B_{0.2}$	258	4	35*	—	12	1.9	3.3	15.2	12.8	13.7	16.7	1100	36
$Ni_{35.5}Co_{14.5}Mn_{35}Ti_{15}$	294	1	24.2*	1.6	4.2*	4.2	5.8	8.5	6.6	12.2	10.6	175	37
$Pd_{59.3}In_{23.2}Fe_{17.5}$	265	4	16	0.32	—	—	2.1	—	15.4	16.7	11.8	171	38
$Co_{50}Fe_{2.5}V_{31.5}Ga_{16}$	283	5	31*	0.7	10*	2.45	2.6	9	8.4	12.9	12.3	518	39
$Mn_{0.6}Fe_{0.4}NiGe_{0.5}Si_{0.5}$	319	6	18.2	−2.8	—	−7.4	−7.3	14.5	13.3	11.2	8	81	40
$Gd_5Si_2Ge_2$	262	2.9	13.4*	0.3	1.3*(d)	3.2	3.8	7.7	4.7	16	16	149	41 and 42
$Fe_{49}Rh_{51}$	319	2.5	12.5*	1	8.1*	5.4	6.4	9.6	7.8	7.5	6.4	172	43 and 44
$LaFe_{11.33}Co_{0.47}Si_{1.2}$	250	2.1	8.6	−1	2.2(d)	—	−7.3	—	—	38.1	32.9	183	20
$La(Fe_{0.92}Co_{0.08})_{11.9}Si_{1.1}$	304	9	19.3*	−1.5	—	−6.8	−7	4.4	5.2	36.3	11.5	516	45
$MnCoGe_{0.99}In_{0.01}$	308	3	51	−3.9	—	−7.7	−7.6	8	—	32.9	41	1436	46
$MnCoGeB_{0.03}$	287	4.8	36.1*	−4	15*	−10	−10	13.4	8.4	17.9	12.1	1464	47
$(MnCoGe)_{0.96}$-$(CuCoSn)_{0.04}$	303	0.9	32.6	−3.9	7.7	−8.8	−11.8	14.1	17.1	24.1	25.4	383	48
$MnNi_{0.77}Fe_{0.23}Ge$	266	1.1	23	−2.7	—	−14.4	−15.1	10.6	8.7	—	—	46.3	49
$(MnNiSi)_{0.6}(FeCoGe)_{0.4}$	274	2.7	47*	−2.8	4*	−7.7	−6.8	16.9	14.1	13.6	15.1	244*	50
Mn_3GaN	290	1.39	22.3	−1	4.8	—	−6.5	—	—	7.8	8.4	199	51
Mn_3NiN	253	0.56	35	−0.4	5.8	−1.3	−1.3	8	7	7.4	5.8	268	52
Mn_3PdN	282	4.9	28.3*	−0.2	6*	−1.4	−1.2	2.3	1.4	6.3	4.9	95*	53
$Mn_3Zn_{0.5}In_{0.5}N$	300	4.2	20	−0.9	8.5	−3.1	−3.3	8.9	8.4	27	23	142	54

[a] (T) phase transition temperature during cooling (for the inverse BCE) and heating (for the conventional BCE) processes; (p) maximum applied hydrostatic pressure in the reported materials; $\lvert\Delta S_{it}\rvert$, $\lvert\Delta T_{ad}\rvert$ and RC are the absolute value of the isothermal entropy change, the absolute value of the adiabatic temperature change, and refrigeration capacity under the maximum reported application pressure, respectively; ($\Delta\omega$) is the volume change rate (heating); $[(dT/dp)_h]$ is the barocaloric coefficient during heating; $[(dT/dp)_c]$ is the barocaloric coefficient during cooling; (ΔT_{hys}) is thermal hysteresis of the phase transition at atmospheric pressure; (ΔT^{p}_{hys}) is thermal hysteresis at maximum applied hydrostatic pressure; (ΔT_{width}) is the width of the phase transition at atmospheric pressure; (ΔT^{p}_{width}) is the width of the phase transition under maximum applied hydrostatic pressure. Values of $\lvert\Delta S_{it}\rvert$, $\lvert\Delta T_{ad}\rvert$ and RC marked with an "*" indicate that these values are reversible. The values of $\lvert\Delta T_{ad}\rvert$ followed by (i) are derived using the formula $\lvert\Delta T_{ad}\rvert = \lvert T\,\Delta S_{it}/C_p\rvert$ through indirect methods, and those followed by (d) indicate that they are obtained by direct measurement, and values without any designation are obtained through quasi-direct methods $(\Delta T_{ad}(T,p) = T(S,p) - T_{ad}(S,0)$.

Table 2 Physical parameters of the giant (colossal) barocaloric effect in ionic compounds, organic–inorganic hybrid materials, and organic compounds[a]

	Materials	T [K]	p [kbar]	$\lvert\Delta S_{it}\rvert$ [J kg^{-1} K^{-1}]	$\Delta\omega$ [%]	$\lvert\Delta T_{ad}\rvert$ [K]	$(dT/dp)_h$ [K kbar^{-1}]	$(dT/dp)_c$ [K kbar^{-1}]	ΔT_{hys} [K]	ΔT_{hys}^{p} [K]	T_{width} [K]	ΔT_{width}^{p} [K]	RC [J kg^{-1}]	Ref.
Ionic compounds	$Ni_{0.85}Fe_{0.15}S$	297	1	52.8*	−2	8*	−8.1	−5	11.2	8.3	8.7	9.2	441	58
	AgI	407	2.5	60*	−5	18*	−14	−12.8	24	18	15.4	10.6	1085*	59
	$(NH_4)_2SO_4$	222	2.5	60*	−0.5	8*	−5.5	−4.4	4.2	1.4	4.6	2.5	276	60
	NH_4HSO_4	160	1.5	68	—	10	—	−12.3	—	—	13	9.2	1240	61 and 62
	NH_4I	268	0.8	71*	16.9	34(i)	79	81	26.1	21.8	13.6	10.2	3046*	63
	$BaTiO_3$	400	2.5	1.6	−0.11	3	−5.8	−5.4	0.7	2.3	9.2	7.2	15.5	64 and 65
	$NdCu_3Fe4O_{12}$	300	5.1	65.1	−1.7	13.7	—	−3.6	—	—	24.8	27.6	1205	66
	NH_4SCN	335	1	128.7	—	26(i)	−30	−25.8	28	23	7.2	—	3755	67
	KPF_6	262	0.9	144	—	—	22.6	9.8	—	—	—	—	—	68
	Cyano-RbMnFeCo	251	5.6	169*	—	44* (d)	—	—	55	76	18.4	15.2	26 000*	69
Organic–inorganic hybrid materials	[TPrA][Mn(dca)$_3$]	332	0.07	30.5*	1.25	4.1*	19.7	23.1	2.8	2.6	4.5	4.1	479*	5
	[TPrA]Cd[dca]$_3$	386	0.07	11.5*	0.4	—	38.2	38.2	1.3	1.3	1.2	1.2	14*	70
	$[Fe(hyptrz)_3]A_2 \cdot H_2O$	273	5	56	—	10	—	33.2	—	—	—	—	1223	71
	$Fe_3(bntrz)_6(tcnset)_6$	318	2.6	120*	2.9	35*	25.1	23.7	1.4	3.7	9.2	14.5	7496*	72
	$(C_{10}H_{21}NH_3)_2MnCl_4$	311	2.5	250*	7	12*	25	28	8.2	5.8	10.9	11.2	8373*	31
	$[(CH_3)_4N]Mn[N_3]_3$	308	1.1	70*	1.5	—	12	12	6.7	6	6.6	6	468*	73
	$[FeL_2][BF_4]_2$	264	4.3	76	2.6	4.5	—	15.2	4	5.3	7.6	5.1	—	30
	$Fe[HB(tz)_3]_2$	332	0.15	92*	3.6	2.1*	21.5	21.4	1.2	1.2	1.4	1.4	173*	74
	$(DA)_2MnCl_4$	311	0.5	248*	8	6.9*	22.5	20.2	3.4	3.3	4.1	3.7	1340*	75
	$(NA)_2CuBr_4$	306	0.5	91.3*	4	9.4*	26.7	26.7	1.8	1.6	2.6	2.7	766*	75
	$[Fe(L)(NCS)_2]$	265	1	114.4*	2.5	15.9*	18	18.8	2	—	13.6	—	2079*	76
	$CH(NH_2)_2I$	345	1	50*	—	24(i)	9.7	9.3	6.4	6.7	5.6	5.1	178*	77
	[DBA][BF_4]	269	1	237.7*	8.4	17*	29	29	4.2	5.9	9.5	9.6	4031*	78
	$[Cp_2Fe][PF_6]$	347	1	57*	2.2	16*	28.1	27.6	3.3	3.7	9.1	9.4	1363*	79
	$[Cp_2Co][PF_6]$	312	1	55*	2	12*	24	21.7	3.3	5.3	8.2	10	1024*	79
	$(CH_3)_2NH_2Mg(HCOO)_3$	267	2	39.9*	0.36	8.1*	−4.5	−4	7.5	3.4	10.1	9	257*	80
	$[(CH_3)_3(CH_2Cl)N]FeCl_4$	326	0.8	123*	—	—	19.1	19.7	5.9	5.5	8.9	8.1	1204*	81
	$[(CH_3)_3S]FeCl_4$	315	1	125*	—	—	19.2	19.9	12.2	5.5	8.7	8.2	853*	81
	$C_7H_{14}NReO_4$	344	2.8	42*	—	15*	13.8	13.7	7.2	7.1	11	9.9	—	82
	$N(CH_3)_4[FeCl_4]$	384	2.2	112*	—	41*	40	38	8	9.5	10.8	10.9	8403*	82
	$(CH_3–(CH_2)_9)_2NH_2Cl$	325	1	400*	12	11*(d)	19	19.1	7.7	7.4	9.4	8.2	4074*	83
	$(C_6H_{13})_2NH_2Br$	293	0.15	297*	—	59(i)	27.1	27.1	5.6	5.6	2.2	2.2	1218*	84
	$LiCB_{11}H_{12}$	380	2.3	280*	10	32*	31	30	12	16	27	34	14 778*	85
	MOF-508b	298	0.026	438*	14.4	30	—	—	—	—	—	—	—	86
	MIL-53(Al)	298	0.016	311*	—	—	—	—	—	—	—	—	—	87
Organic compounds	NPG	320	5.2	500*	4.9	30*	11.3	9.3	20	22.7	8.4	9.1	24 138	88
	TRIS	406	2.5	682	—	8	3.7	1.5	75.6	65.5	47.1	39.8	15 919	21
	PG	354	2.4	490*	—	10*	7.9	9.4	3.7	27.3	36.9	35.4	4948*	21
	AMP	352	2.5	632	—	16	6.4	8.5	—	67.8	25.4	31.4	10 596	21
	NPA	231	5.9	470*	—	42*	22	19.9	20.3	42.5	9.4	12.8	20 492*	21
	$C_{16}H_{34}$	292	1.5	742*	—	57*	31	26.5	6.1	12.2	5.2	4.8	23 988*	29
	$C_{18}H_{38}$	303	2.3	686*	—	45*	28	26.1	4.1	8.1	3.5	2.9	34 487*	29
	$C_{10}H_{15}Br$	254	2.5	220*	—	55*	35.5	33.3	8.6	18.4	6.8	8.6	10 957*	89
	$C_{10}H_{15}Cl$	316	2.4	208*	—	43*	27.4	27	8.4	11.8	11.7	12.2	14 542*	89
	$C_2B_{10}H_{12}$(o-c)	276	0.6	79*	—	14(i)	30	33	8	7	8.7	7.3	880*	28

Table 2 (*Contd.*)

Materials	T [K]	p [kbar]	$\lvert\Delta S_{it}\rvert$ [J kg^{-1} K^{-1}]	$\Delta\omega$ [%]	$\lvert\Delta T_{ad}\rvert$ [K]	$(dT/dp)_h$ [K kbar^{-1}]	$(dT/dp)_c$ [K kbar^{-1}]	ΔT_{hys} [K]	ΔT^p_{hys} [K]	T_{width} [K]	ΔT^p_{width} [K]	RC [J kg^{-1}]	Ref.
PEG10000/PET15000	334	1	426	—	—	8.8	9.7	21.6	21	24	24	3511	90
$C_{11}H_{18}O$	375	2.5	430*	—	40*	24.1	22.2	10.8	17.3	12	14.4	19 770*	91
$NO_2C(CH_3)_2CH_2OH$	313	5	450*	3.8	19*	6.7	5.8	9.4	12.8	11.1	9.2	16 874*	92
$C_{12}H_{24}O_2$	314	3	600*	—	50*	—	—	—	—	—	—	58 000*	93

[a] (T) phase transition temperature during cooling (for the inverse BCE) and heating (for the conventional BCE) processes; (p) maximum applied hydrostatic pressure in the reported materials; $|\Delta S_{it}|$, $|\Delta T_{ad}|$ and RC are the absolute value of the isothermal entropy change, the absolute value of the adiabatic temperature change, and refrigeration capacity under the maximum reported application pressure, respectively; ($\Delta\omega$) is the volume change rate (heating); $[(dT/dp)_h]$ is the barocaloric coefficient during heating; $[(dT/dp)_c]$ is the barocaloric coefficient during cooling; (ΔT_{hys}) is thermal hysteresis of the phase transition at atmospheric pressure; (ΔT^p_{hys}) is thermal hysteresis at maximum applied hydrostatic pressure; (ΔT_{width}) is the width of the phase transition at atmospheric pressure; (ΔT^p_{width}) is the width of the phase transition under maximum applied hydrostatic pressure. Values of $|\Delta S_{it}|$, $|\Delta T_{ad}|$ and RC marked with an "*" indicate that these values are reversible. The values of $|\Delta T_{ad}|$ followed by (i) are derived using the formula $|\Delta T_{ad}| = |T\Delta S_{it}/C_p|$ through indirect methods, those followed by (d) indicate that they are obtained by direct measurement, and values without any designation are obtained through quasi-direct methods ($\Delta T_{ad}(T,p) = T(S,p) - T_{ad}(S,0)$).

24.2 J kg^{-1} K^{-1}), but its sensitivity to pressure increased (dT/dp from 1.9 K kbar^{-1} to 4.2 K kbar^{-1}) (Table 1).

2.1.2 MM′X. In the MM′X family (M and M′ are transition metal elements and X is typically a main group element),[46,50,95] due to the sensitivity of the magnetic exchange interactions and crystallographic symmetry to chemical stress, the magnetic and structural transitions can be influenced by the introduction of small atoms or doping. Interestingly, the fusion of two different compositions of MM′X alloys can result in a stable single phase, known as isostructural alloys (alloys with the same crystal structure), such as MnNiSi–FeCoGe[96] and MnCoGe–CuCoSn.[50] Moreover, alloys with excellent barocaloric performance can be obtained by adjusting the composition ratio between the two alloys.[97]

MnCoGe with a stoichiometric composition does not exhibit a magneto-volume coupling effect.[46] However, the substitution of 1% In for the Ge element ($MnCoGe_{0.99}In_{0.01}$) can enable magneto-volume coupling (from ferromagnetic orthogonal to paramagnetic hexagonal). Additionally, the doping with B atoms ($MnCoGeB_{0.03}$) can also enable magneto-volume coupling.[47] The magneto-volume coupling effect, accompanied by a significant volume change (Table 1), will induce a caloric effect when a magnetic or hydrostatic pressure field is applied. If the external field is a magnetic field (*i.e.*, magnetocaloric effect), a significant volume change ($\Delta\omega \approx -4\%$) can cause alloy fragmentation and mechanical failure during refrigeration. However, in barocaloric refrigeration, this fragmentation of the alloy increases the contact area between the sample and the pressure transfer medium, enhancing heat conduction during the refrigeration process. As shown in Table 1, replacing Ge with a small amount of In can enhance the entropy change of the alloy. However, introducing a small amount of B atoms can improve the pressure sensitivity properties (dT/dp) of the alloy. From these two alloys, chemical modification of these materials can increase the pressure sensitivity of the alloy while sacrificing part of the entropy change and *vice versa*. This behavior is similar to that observed in Ni_2MnZ but is more pronounced in MnCoGe. Alloys that are extremely sensitive to pressure can also be obtained by elemental substitution. In MnNiGe, replacing Ni atoms with Fe atoms ($MnNi_{0.77}Fe_{0.23}Ge$) can achieve magneto-volume coupling, greatly improving the pressure sensitivity of the alloy ($dT/dp \approx -15.1$ K kbar^{-1}).[49] It is unexpected that, when the pressure is increased to 3 kbar, a decoupling effect occurs, resulting in the disappearance of the barocaloric effect.

It is worth noting that alloys with exceptional barocaloric properties can be obtained by fusing single-phase alloys with different proportions. For example, when MnCoGe and CuCoSn are combined in a ratio of 96 : 4, an extremely pressure–sensitive alloy ($dT/dp \approx -11.8$ K kbar^{-1}) is obtained.[48] In the $(MnCoGe)_{0.96}$–$(CuCoSn)_{0.04}$ alloy, only a small pressure ($p \approx 0.3$ kbar) is required to induce a total entropy change. When MnNiSi and FeCoGe are fused in a ratio of 62 : 38, a large isothermal entropy change ($|\Delta S_{it}| \approx 62$ J kg^{-1} K^{-1}) can be achieved.[96] Interestingly, its total transition entropy increases from approximately 62 to 74 J kg^{-1} K^{-1} as the pressure increases from atmosphere pressure to 2.7 kbar. This increase in entropy change with pressure enhances the BCE of the alloy. Fusion of

single-phase alloys can introduce chemical strain, which affects the phase transition temperature similar to the applied pressure.[40] In a study of the isostructural alloy MnNiGe, the modulation of the phase transition by chemical strain and hydrostatic pressure was compared and it is found that the pressure effect with $p \approx 18.8$ kbar was equivalent to the phase transition shift induced by replacing 10% of Mn with Fe.

2.1.3 Anti-perovskite M_3XA. Anti-perovskite M_3XA materials (where M is a transition metal, X is a metal, and A is an element such as C, N, or B) belong to a large family of itinerant electron systems. In anti-perovskites, volume and magnetic transitions are coupled.[51,52] Some anti-perovskites undergo a magnetic transition from antiferromagnetic (AFM) to paramagnetic (PM) accompanied by a negative volume change, such as Mn_3GaN,[51] Mn_3NiN,[52] and Mn_3PdN.[53] This type of transition is difficult to induce using a magnetic field. However, the strong magneto-volume coupling effect enables their induction by pressure.

Mn_3GaN undergoes a magnetic transition from a Γ^{5g} AFM state to a PM state.[98] In the Γ^{5g} AFM state, spin frustration can enhance the BCE of materials compared to systems without spin frustration.[51,99,100] In the frustrated system, the BCE is positively related to $\Delta\omega|dT/dp|^{-1}$. $\Delta\omega|dT/dp|^{-1}$ for Mn_3ZnN, Mn_3InN and $Mn_3Zn_{0.5}In_{0.5}N$ is 2.1, 0.9 and 2.9 respectively.[54] From the $\Delta\omega|dT/dp|^{-1}$, the barocaloric performance of $Mn_3Zn_{0.5}In_{0.5}N$ is better than that of Mn_3ZnN and Mn_3InN. The isothermal entropy change of Mn_3ZnN and Mn_3InN is 32 J kg^{-1} K^{-1} and 12 J kg^{-1} K^{-1}, respectively. The isothermal entropy of $Mn_3Zn_{0.5}In_{0.5}N$ is 37 J kg^{-1} K^{-1}, which is greater than that of Mn_3ZnN and Mn_3InN. For Mn_3GaN, Mn_3PdN and Mn_3NiN, $\Delta\omega|dT/dp|^{-1}$ is 1.53, 1.55 and 3, respectively.[51–53] The BCE of Mn_3NiN is more pronounced than that of Mn_3GaN. In Mn_3NiN, as the magnetic moment rotates within the (111) plane from Γ^{5g} AFM to Γ^{4g} AFM near the phase transition temperature, Mn_3NiN exhibits a pressure-induced isothermal entropy change ($|\Delta S_{it}| \approx 35$ J kg^{-1} K^{-1}) and adiabatic temperature change ($|\Delta T_{ad}| \approx 5.8$ K). The giant BCE originates from multisite exchange interactions among the Mn magnetic moments and their coupling with itinerant electron spins.

2.1.4 Others. $LaFe_{13}Si$,[101–103] $Gd_5Si_2Ge_2$,[104] and $Fe_{49}Rh_{51}$ (ref. 105 and 106) are well-known magnetocaloric materials. Due to their strong magneto-volume coupling effect, these alloys respond to pressure.[107–110] $LaFe_{13-x}Si_x$ exhibits a $NaZn_{13}$ structure in the concentration range of $1.2 \leq x \leq 2.5$. When $x = 1.2$ and Fe is replaced by Co, $LaFe_{11.33}Co_{0.47}Si_{1.2}$ is obtained.[20] $LaFe_{11.33}Co_{0.47}Si_{1.2}$ undergoes a first-order phase transition from the ferromagnetic phase to the paramagnetic phase. Spin fluctuation produces a negative contribution to volume, resulting in negative thermal expansion. $LaFe_{11.33}Co_{0.47}Si_{1.2}$ exhibits an inverse BCE, which is experimentally demonstrated by measuring the temperature change. This is manifested by the material heating up when hydrostatic pressure is removed. In the $LaFe_{13-x}Si_x$ system, research conducted on the high-pressure effect in La $(Fe_{0.92}Co_{0.08})_{11.9}Si_{1.1}$ and the results suggested that the isothermal entropy change increased nearly threefold under 9 kbar compared to the entropy change at atmospheric pressure.[45] Additionally, the phase transition became sharper as pressure increased. When chemical stress was applied to the material by injecting H atoms, introducing H atoms can change the phase transition temperature but cannot make the phase transition sharper. Neutron diffraction study under high pressure showed that hydrostatic pressure acting on the Fe–Fe bond length of the internal icosahedron resulted in a shorter Fe–Fe bond length, causing a sharper phase transition. Based on the above results, it is evident that although both methods can shift the phase transition, their effects are somewhat different.

Applying hydrostatic pressure or a magnetic field to $Gd_5Si_2Ge_2$ reveals that both the barocaloric and magnetocaloric effects are conventional caloric effects, determined by direct measurement of the temperature change.[42] $Gd_5Si_2Ge_2$ undergoes a first-order phase transition from a high-temperature monoclinic paramagnetic phase to a low-temperature orthogonal ferromagnetic phase.[41] This suggests that both high pressure and high magnetic fields can stabilize the smaller-volume orthogonal ferromagnetic phase in $Gd_5Si_2Ge_2$.[111] When a magnetic or pressure field is applied to $Fe_{49}Rh_{51}$ with an AFM to ferromagnetic (FM) transition, it exhibits a conventional BCE and an inverse magnetocaloric effect. This is mainly because pressure stabilizes the small-volume AFM phase while the magnetic field stabilizes the FM phase. In $Fe_{49}Rh_{51}$, the antiferromagnetic to ferromagnetic transition occurs without a change in crystal symmetry, but the strong magnetic volume coupling effect causes a volume change resulting in a giant BCE during the magnetic phase transition.[43] Applying a relatively small pressure can induce a significant caloric effect with $|\Delta T_{ad}| \approx 8.1$ K in $Fe_{49}Rh_{51}$.

2.2 Ionic compounds

Compounds composed of cations (cationic groups) and anions (anionic groups) are classified as ionic compounds. Among these, phase transition types mainly include ionic order transitions, and ferroelectric or ferromagnetic phase transitions.[112,113] The presence of negative thermal expansion, associated with ferromagnetic or ferroelectric phase transitions, can induce an inverse BCE in ionic compounds, such as in NiS,[58] $BaTiO_3$ (ref. 64 and 114) and $(NH_4)_2SO_4$.[60] Based on the structural units, ionic compounds can be classified into 3D framework materials with three-dimensional network atomic frameworks and molecular crystals composed of molecules.

2.2.1 3D framework materials. In ionic compounds, the BCE was first investigated in perovskite materials, which exhibit excellent physical properties.[115,116] To date, giant barocaloric effects have been observed in many perovskite materials, such as manganates, titanates, and nickelates. Nickelates are the earliest reported barocaloric materials among perovskites. The study of $Pr_{12-x}La_xNiO_3$ shows that it can be used for cryogenic cooling.[23,117] Then, the BCE of titanates and manganates was reported, such as $La_{0.7}Pb_{0.3}MnO_3$,[117] $Pb_{0.99}Nb_{0.02}(Zr_{0.95}Ti_{0.05})_{0.08}O_3$,[118] and $BaTiO_3$.[64,65] The most well-known material is the ferroelectric ceramic $BaTiO_3$, which undergoes first-order phase transitions at 400 K (cubic to tetragonal) and 280 K (tetragonal to orthorhombic), respectively. Both phase

transitions are particularly sensitive to pressure. These two phase transitions of $BaTiO_3$ are both inverse BCE. As pressure increases, the two first-order phase transitions shift to lower temperatures. The A-site-ordered quadruple perovskite-structure oxides, represented as $AA'_3B_4O_{12}$, are one class of the perovskite materials.[119] In $NdCu_3Fe_4O_{12}$, an entropy change ($|\Delta S_{it}| \approx 65.1$ J kg^{-1} K^{-1}) and adiabatic temperature change of 13.7 K is obtained, when applying a hydrostatic pressure of 5.1 kbar. The large negative thermal expansion and magnetic ordering change due to inter-site charge transfer between Cu and Fe contribute significantly to the total entropy change and a colossal latent heat of 25.5 kJ kg^{-1}.[66]

In certain ionic compounds comprising transition metal elements and main-group nonmetals, the barocaloric effect is significant.[120,121] For example, AgI[59] and NiS[58] demonstrate outstanding barocaloric properties. The crystal structure of the superionic conductor AgI undergoes a phase transition from α-AgI to γ-AgI and β-AgI phase ($\alpha \leftrightarrow \beta + \gamma$), resulting in a giant BCE due to the increase/decrease in entropy through the melting/dissolution of the interstitial sublattice of silver cations.[59] Applying hydrostatic pressure ($p \approx 2.5$ kbar) can induce a significant isothermal entropy change ($|\Delta S_{it}| \approx 60$ J kg^{-1} K^{-1}) and an adiabatic temperature change ($|\Delta T_{ad}| \approx 18$ K). The first-order phase transition in AgI is associated with a substantial volume contraction ($\Delta\omega \approx -5\%$). In the case of NiS, it is reported that the barocaloric effect can be enhanced by tuning the electronic structure.[58] NiS undergoes a first-order phase transition from an antiferromagnetic non-metallic state to a ferromagnetic metallic state. To improve the contribution of electron entropy to the BCE, the electronic structure of NiS was modified by partially replacing Ni with Fe. In $Ni_{1-x}Fe_xS$, as x increases, the pressure-induced entropy change under 1 kbar gradually increases, reaching a maximum ($|\Delta S_{it}| \approx 52.8$ J kg^{-1} K^{-1}) when $x = 0.15$. Moreover, adjusting the electronic structure of NiS effectively augments both the electronic entropy and the thermal conductivity of the material. High thermal conductivity can improve heat transport efficiency in the refrigeration cycle. Thus, manipulating the electronic structure offers a novel approach to study the BCE.

Cyano-RbMnFeCo is a cyano-bridged rubidium–manganese–iron–cobalt ternary metal assembly.[69] Its barocaloric effect originates from the contributions of spin–orbital entropy and vibrational entropy, accompanied by charge transfer. This material exhibits significant reversible barocaloric effects under various pressures, with large reversible adiabatic temperature changes ($|\Delta T_{ad}| \approx 44$ K), as well as excellent performance in reversible cooling capacity (RC ≈ 26 000 under 5.6 kbar) and temperature window (85 K under 5.6 kbar) parameters. Thermocouple measurements show substantial temperature changes during compression (44 K) and decompression (31 K). Even after multiple cycles (up to 103 times), its performance remains stable. Its high thermal conductivity (20.4 W m^{-1} K^{-1}) makes it suitable for high-frequency operation in barocaloric devices. The low driving pressure and wide temperature window provide considerable advantages for refrigeration applications, enabling large-span instant temperature changes. Additionally, by adjusting the cobalt content, it can better match the operating temperature.

$[MO_xF_{6-x}]^{n-}$ (where $x = 1$, 2, 3 and M = Nb, Mo, W, Ti, *etc.*) belongs to a non-centrosymmetric ionic group.[122–124] It can combine with metal cations or $(NH_4)^+$ to form compounds. In $(NH_4)_2NbOF_5$ and $(NH_4)_2TiOF_4$, the phase transition is unstable under pressure, but has little effect on the BCE of these materials.[125–128] Applying a small pressure can induce the phase transition to split into two first-order phase transitions (three phase points under pressure). However, the total entropy change of the phase transition remains almost unchanged and the maximum entropy change is as high as 100 J kg^{-1} K^{-1}. Some materials in this class are particularly sensitive to pressure. K_2TaF_7 is extremely sensitive to pressure ($dT/dp \approx -22$ K kbar^{-1}).[129] Although its phase transition occurs at a high temperature (486 K), the significant pressure sensitivity can induce a phase transition at room temperature for refrigeration purposes.

2.2.2 Molecular crystals. Ammonium-based materials are extensively studied within the class of ionic compounds. The BCE in these materials arises from their structural characteristics or the ferroelectric phase transition.[130] The ferroelectric material $(NH_4)_2SO_4$[131,132] undergoes a first-order phase transition from a disordered phase to a ferroelectric ordered phase accompanied by a large volume change. Application of a hydrostatic pressure of approximately 1 kbar to $(NH_4)_2SO_4$ induces a significant isothermal entropy change ($|\Delta S_{it}| \approx 60$ J kg^{-1} K^{-1}). With increasing pressure, the magnitude of the entropy change progressively diminishes. This occurs as the sign of the entropy change induced by pressure is opposite to that associated with the phase transition entropy. The well-recognized ferroelectric material NH_4HSO_4 demonstrates a remarkable BCE, attributed to two first-order phase transitions: $P2_1/c$ (271 K) ↔ Pc (160 K) ↔ $P1$.[61,62] Among the two phase transitions, the larger value of isothermal entropy change is 68 J kg^{-1} K^{-1} at 160 K corresponding to the $Pc \leftrightarrow P1$ transition. Both of the phase transitions are sensitive to pressure as dT/dp is 9 K kbar^{-1} and -12.3 K kbar^{-1} at 271 K and 160 K, respectively. It is observed that the values of dT/dp for the two phase transitions have opposite signs. Hence, inverse and conventional BCE coexist in NH_4HSO_4. Unlike the above two materials, NH_4I, while not displaying ferroelectric properties, undergoes a series of complex structural transitions.[63] NH_4I undergoes successive phase transitions from a low-temperature tetragonal γ-phase ($P4/nmm$) to an intermediate cubic β-phase ($Pm\bar{3}m$), and then to another cubic α-phase ($Fm\bar{3}m$). The phase transition temperature of NH_4I increases at a rate of 79 K kbar^{-1} under pressure. According to available data, the dT/dp value of NH_4I is the highest reported value for barocaloric materials. Neutron scattering studies have revealed that the exceptional barocaloric performance and the marked pressure sensitivity of NH_4I are attributed to the configurational entropy changes in the $[NH_4]^+$ tetrahedra and the significant coupling between reorientation and vibration.

2.3 Organic–inorganic hybrid materials

A compound consisting of short molecular organic chains and metal atoms (or inorganic ionic groups) is categorized as an

organic–inorganic hybrid material.[83,133,134] The BCE of such materials is typically induced by the order–disorder phase transition of the organic chain or the spin-state transition of the metal. In some organic–inorganic materials, it is observed that a relatively modest driving pressure can trigger a giant BCE, and the pressure to trigger such a BCE is comparable to that of traditional vapor compression refrigeration systems.[5,70] Furthermore, a colossal BCE is observed in certain organic–inorganic materials, such as $Fe_3(bntrz)_6(tcnset)_6$,[72] $(DA)_2MnCl_4$ (ref. 75) and $(C_{10}H_{21}NH_3)_2MnCl_4$.[31,135]

2.3.1 3D perovskites. Certain organic–inorganic hybrid materials also exhibit perovskite-type structures.[136–138] Organic–inorganic hybrid perovskites are characterized by the ABX_3 formula, where A denotes an alkylamine cation, B denotes a metal cation, and X denotes a halogen anion or a complex bidentate ligand. There are some organic–inorganic hybrid perovskite materials that exhibit pronounced pressure sensitivity. In $[TPrA][Mn(dca)_3]$[5] and $[TPrA]Cd[dca]_3$,[70] the phase transitions in these materials demonstrate high pressure sensitivity (23.1 K $kbar^{-1}$ and 38.2 K $kbar^{-1}$, respectively). By the application of a modest hydrostatic pressure of 70 bar to $[TPrA][Mn(dca)_3]$ and $[TPrA]Cd[dca]_3$, an isothermal entropy change of 37 J kg^{-1} $K^{-1}$and 11.5 J kg^{-1} K^{-1}, respectively, can be achieved. The BCE in these materials arises from the complex structural transition caused by the order–disorder transition of the organic groups and the synergistic association of the off-center displacements of the TPrA cations. The driving pressure required for these two materials is the smallest among that of the reported materials. In the perovskite-like structure of $(CH_3)_2NH_2Mg(HCOO)_3$, MgO_6 octahedra are linked by $HCOO^-$ ligands to form a framework, with $[(CH_3)_2NH_2]^+$ cations filling the voids.[80] During the first-order phase transition, a discontinuous negative volume change occurs, indicating an inverse barocaloric effect. With increasing pressure, the discontinuous volume change and entropy change both decrease, and at 4 kbar, the transition becomes continuous, forming a triple point. The triple point arises from the compression of cation-containing voids. Although the volume change is continuous, a significant transformation entropy is still retained. Therefore, the material exhibits promising potential for barocaloric cooling applications.

2.3.2 2D perovskites. Two-dimensional perovskites, such as $(DA)_2MnCl_4$ (DA = decyl-ammonium), $(NA)_2CuBr_4$ (NA = nonyl-ammonium) and $(C_6H_{13})_2NH_2X$ (X = Cl, Br, I), exhibit remarkable advantages including high pressure sensitivity, minimal hysteresis, and large entropy change.[75,84] $(DA)_2MnCl_4$ undergoes a phase transition from an ordered monoclinic structure with bilayers of hydrocarbon chains to an expanded orthorhombic lattice with disordered hydrocarbon chains, which results in a maximum achievable reversible isothermal entropy change ($|\Delta S_{it}| \approx 248$ J kg^{-1} K^{-1}) at an operating pressure of 0.5 kbar. The entropy change is attributed to reorientation of the alkylammonium cations between favorable orientations within the Mn–Cl pockets and internal rotations of C–C bonds. Layer-structured hybrid organic–inorganic $(C_{10}H_{21}NH_3)_2MnCl_4$ undergoes a structural transformation from monoclinic into tetragonal, with a reversible colossal BCE ($|\Delta S_{it}| \approx 250$ J kg^{-1} K^{-1}) being produced upon applying a small pressure (below 1 kbar).[31] The large phase transition entropy is attributed to the drastic transformation of the organic chains from ordered rigidity into disordered flexibility within the metallic frame. The temperature of the phase transition of this material is sensitive to pressure ($dT/dp \approx 28$ K $kbar^{-1}$) attributable to the significant volume change ($\Delta\omega \approx 7\%$) and strong disorder of the organic chain. To understand the mechanism, temperature-variable single-crystal XRD was performed on single crystals of $(C_{10}H_{21}NH_3)_2MnCl_4$.[135] The results indicated that the alignment of $MnCl_6$ octahedra twists seriously at the low-temperature state due to strong hydrogen bonding between the organic and inorganic groups. At high-temperature, $MnCl_6$ octahedra are arranged regularly, indicating weakened hydrogen bond interaction.

2.3.3 Spin-crossover materials. The phase transition of spin-crossover materials is a spin transition between high-spin and low-spin states.[139,140] The pressure required for the phase transition of such materials is generally small. High-pressure calorimetry studies on the spin-crossover material Fe $[HB(tz)_3]_2$ indicate a measurable entropy change at a pressure as low as 10 bar.[74] The application of a hydrostatic pressure of 150 bar results in an isothermal entropy change of 99 J kg^{-1} K^{-1} and an adiabatic temperature change of 2 K. In $[FeL_2]$ $[BF_4]_2$, and only an applied hydrostatic pressure of 300 bar can induce a 3 K adiabatic temperature change.[30] Spin-crossover molecular crystal $[FeL_2]$ $[BF_4]_2$ undergoes a first-order phase transition between its diamagnetic $S = 0$ ground state and a high spin paramagnetic $S = 2$ state. For $[Fe(hyptrz)_3]$ $A_2 \cdot H_2O$, the application of a pressure $p \approx 0.9$ kbar can result in an isothermal entropy change ($|\Delta S_{it}| \approx 56$ J kg^{-1} K^{-1}).[71] The transition between high and low spin states is accompanied by large thermal expansion, which contributes to a significant lattice entropy change. The strong coupling between the lattice and electronic states of low or high spin in Fe^{2+} N_6 cores leads to a giant BCE. The trinuclear spin-crossover material $Fe_3(bntrz)_6(tcnset)_6$ undergoes a spin-state transition between FeII high and low spin states under pressure, exhibiting a colossal BCE with an $|\Delta S_{it}|$ value of approximately 120 J kg^{-1} K^{-1} when a pressure of $p \approx 2.6$ kbar is applied.[72] This material also exhibits a broad phase transition temperature range of approximately 60 K and negligible thermal hysteresis.

2.3.4 Hybrid plastic crystals. Hybrid ionic plastic crystals consist of discrete inorganic anions (such as $FeCl_4^-$) and organic cations (such as $[(CH_3)_3(CH_2Cl)\ N]^+$ and $[(CH_3)_3S]^+$).[81] The relatively weak electrostatic interactions between organic cations and inorganic anions result in a structure with specific structural units. Due to the weak chemical interactions and flexible nature of the organic cations, the ionic interactions and structural transitions are easily induced under pressure, leading to changes in the thermal properties of the material and generating barocaloric effects. Additionally, the impact of inorganic anions on properties such as density contributes to more compact refrigeration applications. Composed of specific organic cations (such as $C_7H_{14}N^+$ and $N(CH_3)_4^+$) and inorganic anions (such as $NReO_4^-$ and $FeCl_4^-$), the material exhibits structural characteristics of plastic crystal phases at high temperatures and ferroelectric phases at low temperatures.[82]

The molecules display distinct arrangement and motion characteristics in different phases. During the phase transition from the ferroelectric to the plastic crystal phase, molecular structural transitions occur, including rotational jumps at equilibrium positions and changes in intermolecular interactions. These transitions lead to entropy and volume changes, thereby generating barocaloric effects. Due to its unique structure, the ferroelectric plastic crystal material has specific characteristics in barocaloric performance. Although some parameters are not optimal, the reversible adiabatic temperature change demonstrates potential for applications. $LiCB_{11}H_{12}$ belongs to the family of *closo*-borate materials, exhibiting characteristics of plastic crystals and superionic conductors at high temperatures, with molecular reorientation motion and ion diffusion.[85] The order–disorder phase transition at around 380 K induces a barocaloric effect, where lattice vibrations contribute the most to the entropy change, followed by molecular reorientation. Although lithium-ion diffusion contributes minimally on its own, it is crucial for stabilizing the orientational disorder. $LiCB_{11}H_{12}$ demonstrates excellent barocaloric performance, with a reversible entropy change of approximately 280 J kg^{-1} K^{-1} and an adiabatic temperature change of around 32 K at 2.3 kbar, and a reversible entropy change of approximately 200 J kg^{-1} K^{-1} and an adiabatic temperature change of around 10 K at 1 kbar.

2.3.5 Alkylammonium halides. Dialkylammonium halide salts exhibit a structure analogous to that of two-dimensional perovskites. Their general formula is $(C_nH_{2n+1})_2NH_2X$ (X = Cl, Br, I), and they can be derived from $(C_nH_{2n+1}NH_3)_2MX_4$ through the removal of metal cations and other operations.[84] These compounds feature bilayers of hydrocarbon chains, which are confined through hydrogen bonding interactions with two-dimensional sheets of halide anions. The conformational flexibility and softness of the weakly confined hydrocarbons lead to solid-state order–disorder transitions, resulting in significant entropy transitions ($|\Delta S_{it}| \approx 297$ kg^{-1} K^{-1}) and high sensitivity to pressure ($dT/dp \approx 27.1$ K $kbar^{-1}$). Together, these factors enable the generation of barocaloric effects at relatively low pressures. The chemical formula of two-dimensional van der Waals alkylammonium halides is $(CH_3–(CH_2)n_{-1})_2NH_2X$ (where X represents a halogen element).[83] Utilizing long carbon chains results in a two-dimensional structure, characterized by weak van der Waals forces between layers and strong in-plane hydrogen bonds perpendicular to the chain extension direction. The origin of its barocaloric effect lies in the phase transition process, where the interlayer van der Waals forces significantly weaken along the carbon chain extension direction, resulting in a substantial increase in the interlayer spacing. This induces a drastic ordered–disordered conformational change in the organic chains. This phenomenon leads to remarkable barocaloric performance, with an entropy change of approximately 400 J kg^{-1} K^{-1} at 0.8 kbar and an adiabatic temperature change of about 11 K at 1 kbar, demonstrating significant advantages.

2.3.6 Metal–organic frameworks. MIL-53 (Al) is a porous hybrid organic–inorganic material with a MOF (Metal–Organic Framework) structure.[87] During the adsorption and desorption of guest molecules, it undergoes a breathing transition from a narrow-pore to a wide-pore phase. This unique structural flexibility lays the foundation for its subsequent thermal performance. The barocaloric effect originates from structural changes induced by the breathing transition during gas adsorption and desorption, along with the thermally induced release of the adsorbate, resulting in a barocaloric effect. This characteristic, which tightly integrates structural and adsorption processes, creates its exceptional barocaloric effect. MOF-508b is a novel solid-state material with a unique structure and excellent barocaloric performance. Its crystal structure exhibits two pressure-induced phase transitions. Compared to MIL-53 (Al), MOF-508b has a thermal change that is 40% higher, operates at pressures as low as ≤26 bar, and within a temperature range of 273–333 K.[86] Additionally, it does not require thermal regeneration and activation processes and has minimal volume change, demonstrating great potential in environmentally friendly refrigeration and heating applications.

2.3.7 Metallocenium salts. The $[Cp_2M][PF_6]$ salt, composed of a sandwich organometallic cation formed by $(C_5H_5)^-$ anions and Fe^{3+} or Co^{3+}, paired with PF_6^- anions, exhibits phase transitions between ordered and disordered states at different temperatures.[79] This phenomenon arises from the unique structure and chemical bonding of the sandwich organometallic cation, which causes changes in the ionic order–disorder state under pressure, thereby generating barocaloric effects. It demonstrates excellent barocaloric performance at relatively low pressures and allows for performance tuning through ionic structure modification.

2.3.8 Others. An ionic compound composed of $[DBA]^+$ (dibutylammonium) cations and $[BF_4]^-$ anions exhibits four phases within the temperature range of 100–300 K, undergoing three order–disorder transitions.[78] These phase transitions are related to the order–disorder transitions of specific groups within the ions, such as the methyl groups and all carbon atoms of the $[DBA]^+$ cation. The structural disorder gradually arising from the $[DBA]^+$ cations and $[BF_4]^-$ anions leads to phase transitions at different temperatures, with the order–disorder transitions in various parts of the ions (*e.g.*, methyl groups and carbon atoms) causing corresponding thermal transitions, thus generating barocaloric effects.

2.4 Organic compounds

Organic compounds can be categorized into two types: chain macromolecular organics (or polymers) and organic small molecular crystals. These materials are primarily composed of elements with smaller atomic numbers, elements such as C, H, and O. The BCE in such materials can be attributed to the transition between ordered and disordered states of the organic chains.

2.4.1 Macromolecular organics without a first-order phase transition. In contrast to other materials, the BCE in organic macromolecules arises from a pressure-induced entropy change without undergoing a first-order phase transition.[141] These materials are known as thermoplastic elastomers.[142] To measure the adiabatic temperature of these materials, pressure

is applied to the organic materials through a quasi-hydrostatic device. Experimental findings demonstrate that many of these materials, such as natural rubber (NR),[143,144] vulcanized natural rubber (V-NR), polydimethylsiloxane rubber (PDMS),[145] and acetoxy silicone rubber (ASR),[146] exhibit a remarkable BCE. In the case of natural rubber, the BCE arises due to the ordering of organic molecular chains under pressure. When natural rubber is subjected to a pressure of 3.9 kbar at an initial temperature of 314 K, it results in a temperature change of approximately 25 K. Moreover, at a pressure of 1.7 kbar and a temperature of 290 K, natural rubber displays a large isothermal entropy change of approximately $|\Delta S_{it}| \approx 60$ J kg^{-1} K^{-1}. Further studies on vulcanized natural rubber and PDMS rubber show that the application of pressure on these two materials induces a significant adiabatic temperature change of 10.2 K (at $T = 293$ K and $p \approx 1.7$ kbar) and 28.5 K (at $T = 283$ K and $p \approx 3.9$ kbar), respectively. Among various rubbers, ASR exhibits the best barocaloric properties. It displays a colossal BCE with a temperature change of $|\Delta T_{ad}| \approx 41.1$ K (at $T = 298$ K and $p \approx 3.9$ kbar) and an entropy change of 182 J kg^{-1} K^{-1}. The colossal BCE in ASR is attributed to the amorphization process, which is unrelated to crystallization and the consequent rearrangement of the polymer chains. With regards to waste tire rubber, although the BCE is slightly weaker compared to that of pure V-NR, the heat exchange rate is faster than that of V-NR.[147]

2.4.2 Macromolecular organics with a first-order phase transition. The BCE is particularly notable in organic molecules undergoing solid–liquid phase transitions. Such materials are more sensitive to pressure and display a larger isothermal entropy change compared to those undergoing solid–solid phase transitions. In *n*-alkanes,[29] a slight pressure increase of approximately 0.5 kbar can induce an isothermal entropy change ($|\Delta S_{it}| \approx 742$ J kg^{-1} K^{-1}) that is comparable to the magnitude achieved by typical vapor compression refrigeration. Raman spectroscopy and theoretical calculations have revealed that, in the solid state, the twisting and random thermal movements of molecular chains are suppressed under pressure, leading to a significant isothermal entropy change. Molecular dynamics simulation has further elucidated that the *n*-alkane $C_{20}H_{42}$ can exhibit a large isothermal entropy change and adiabatic temperature change *via* the reduction of intermolecular potential energy under compressive conditions.[148] Elastic copolymers of ethylene and vinyl acetate represent another example that exhibits a liquid–solid transition.[149] During rapid compression and decompression cycles at 4 kbar, its adiabatic temperature change was directly measured as 29.6 K during compression and −26.9 K during decompression, and a wide range of refrigeration temperatures, up to 110 K, is achieved. To explore the practical application potential of such barocaloric materials with both liquidity and elasticity, a refrigerator employing the solid–liquid phase transition method was designed.[150] This approach eliminates the need for a pressure transfer medium, which can enhance the efficiency of heat transfer. Materials exhibiting solid–liquid phase transitions typically display significant melting entropies.[90,150,151] However, they are unable to act as full solid-state refrigerants.[90] The achievement of a colossal barocaloric effect through the utilization of the high entropy inherited from the significant disorder of the liquid phase in amorphous polyethylene glycol (PEG) has been demonstrated, which is solidified with 5 wt% polyethylene terephthalates (PET). In the PEG10000/PET15000 system, the residual entropy of the amorphous PEG can constitute up to 83% of the entropy of the liquid PEG, leading to a barocaloric entropy change of $|\Delta S_{it}| \approx 426$ J kg^{-1} K^{-1} under a modest pressure of 1 kbar. This exceeds the performance of many other barocaloric materials.

2.4.3 Organic plastic crystals. The most studied among small molecule organic crystals is plastic crystals.[82,152] Plastic crystals exhibit excellent barocaloric properties.[88,91] Notably, the colossal BCE was initially observed in plastic crystals, representing a significant advance in the entropy change of barocaloric materials. Highly disordered solids consist of organic molecules that form crystals through the close packing of their mass centers. Upon cooling, the disordered organic molecules reorient into a preferred configuration, resulting in a significant volume change and isothermal entropy change. For instance, the isothermal entropy change of neopentylglycol is 389 J kg^{-1} K^{-1}, and at that time its caloric effect far exceeded that of other caloric materials.[16] *In situ* neutron scattering experiments under pressure verify that this large isothermal entropy change originates from the reorientation of disordered molecules during the phase transition. Molecular dynamics simulations reveal that the significant barocaloric effect in NPG is related to the reversible order–disorder changes in molecular orientation, with hydrogen bonds playing a crucial role.[153,154] Furthermore, plastic crystals with different configurations have exhibited different barocaloric performances (Table 2).[28] A study on three positional isomers of carboranes revealed that molecular isomerization is an effective means to enhance the BCE. In carboranes with an orthorhombic-to-tetragonal structural transition, a substantial isothermal entropy change can be achieved with an extremely small pressure of 0.6 kbar. Although the BCE of plastic crystals is significant, their thermal conductivity is relatively low.[155,156] In order to improve the thermal conductivity of plastic crystals, NPG was combined with high thermal conductivity graphite nanosheets, significantly enhancing the thermal conductivity of NPG (from 0.42 to 18.4 W m^{-1} K^{-1}).

3 Discussion of the barocaloric properties among materials

To gain a systematic understanding of barocaloric performance, we conducted a detailed investigation of the physical parameters associated with the BCE. We discuss these parameters from two perspectives. First, with respect to the driving pressure field, we performed a comprehensive evaluation and analysis of the minimum reversible pressure, the shift in phase transition temperature with pressure, as well as the refrigeration temperature range. Second, in terms of barocaloric performance, we systematically summarized and comparatively analyzed key parameters of the BCE, including isothermal entropy change, adiabatic temperature change, and refrigeration capacity.

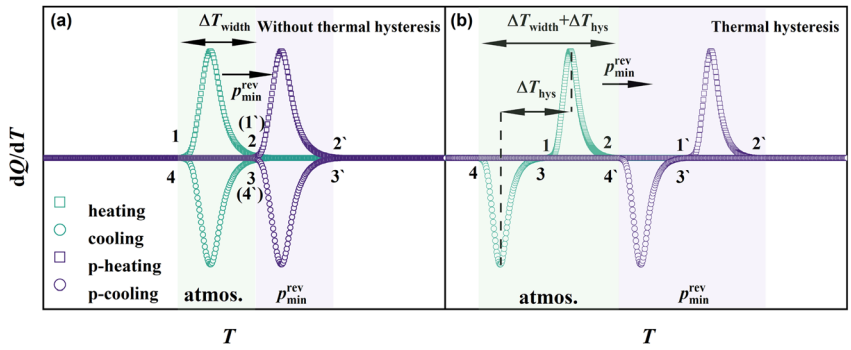

Fig. 2 The minimum reversible driving pressure (p_{min}^{rev}) required for a first-order phase transition in the refrigeration process without thermal hysteresis (a) and with thermal hysteresis (b). Points 1 and 2 correspond to the initial and final states of the transition from the low temperature phase (LTP) to the high temperature phase (HTP) under atmospheric pressure, respectively. Points 3 and 4 correspond to the initial and final states of the transition from the HTP to the LTP under atmospheric pressure, respectively. Points 1′ and 2′ correspond to the initial and final states of the transition from the LTP to the HTP under pressure, respectively. Points 3′ and 4′ correspond to the initial and final states of the transition from the HTP to the LTP under pressure, respectively. In (a), points 2 and 1′ coincide, as do points 3 and 4′. In (b), points 2 and 4′ coincide. The green area shows the endothermic and exothermic curves under atmospheric pressure, while the purple area shows the endothermic and exothermic curves under applied pressure.

The minimum reversible pressure is a critical parameter for evaluating the barocaloric effect. The minimum reversible pressure is the pressure needed to induce a first-order phase transition to complete a refrigeration cycle. Based on the barocaloric coefficient during cooling [$(dT/dp)_c$]and heating [$(dT/dp)_h$] cycles, we can estimate the minimum reversible pressure for barocaloric materials.

In solid-state refrigeration processes, the presence of thermal hysteresis can greatly reduce refrigeration efficiency.[157–159] In the conventional BCE, as shown in Fig. 2, the minimum reversible pressure is defined as the applied pressure that is sufficient to induce a complete transformation from the high temperature phase (HTP) into the low temperature phase (LTP). Upon release, the pressure facilitates a complete

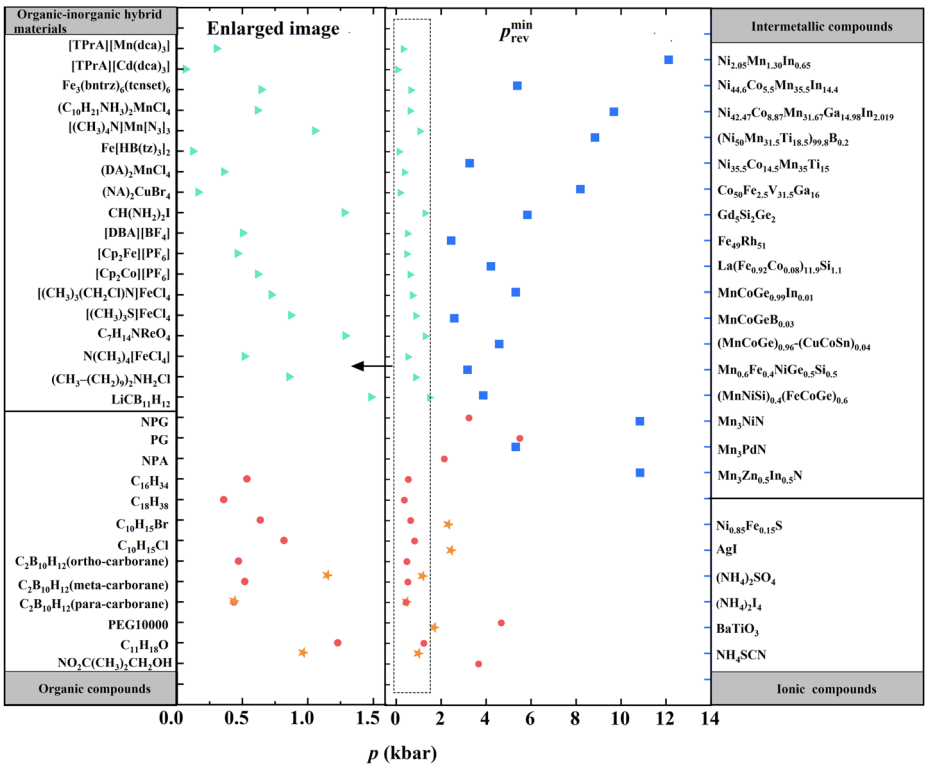

Fig. 3 The minimum reversible pressure necessary for a material to undergo a complete refrigeration cycle. Blue squares (■) denote intermetallic compounds, with the corresponding substances labeled on the right axis. Green triangles (▲) indicate organic–inorganic hybrid materials, orange pentagrams (★) represent ionic compounds, and the red circle (●) represents organic compounds, with the corresponding substances labeled on the left axis.

transformation of the LTP into HTP. Therefore, p^{rev}_{min} without thermal hysteresis (Fig. 2a) can be expressed as $p^{rev}_{min} = \Delta T_{width}/(dT/dp)_c$, while p^{rev}_{min} with thermal hysteresis (Fig. 2b) can be expressed as $p^{rev}_{min} = (\Delta T_{hys} + \Delta T_{width})/(dT/dp)_c$ (where c represents the cooling process). In the conventional BCE, Fig. 2 shows that the value of the minimum reversible pressure is related to the barocaloric coefficient $[(dT/dp)_c]$ during the cooling process. However, in the inverse BCE, the minimum reversible pressure is related to the barocaloric coefficient $[(dT/dp)_h]$ during the heating process.

For the conventional BCE, the equation can be expressed as:[21]

$$p^{rev}_{min} = \left(\Delta T_{hys} + \Delta T_{width}\right) \Big/ \left(\frac{dT}{dp}\right)_c \quad (2)$$

For the inverse BCE, the equation can be expressed as:

$$p^{rev}_{min} = \left(\Delta T_{hys} + \Delta T_{width}\right) \Big/ \left(\frac{dT}{dp}\right)_h \quad (3)$$

A smaller minimum reversible pressure is beneficial for barocaloric refrigeration applications. Therefore, the minimum reversible pressure is an important parameter for screening barocaloric materials. Typically, the barocaloric effect is associated with first-order phase transitions, with the exception of some organic macromolecules such as NR, PDMS, and ASR (the details of this part are in Section 2.4.1). As such, the cost will be low when the minimum reversible pressure is smaller. Based on formulae (2) and (3), we calculated the minimum reversible pressure, as shown in Fig. 3. It should be noted that ΔT_{width} is highly sensitive to measurement methodology and equipment, such as the temperature ramp rate. Different materials have been primarily measured using quasi-direct methods on various equipment, where temperature ramp rates can range from 1 K min^{-1} to 10 K min^{-1} or more. This variability can affect fair comparison across materials. Therefore, this should be considered when comparing ΔT_{width} values. According to eqn (2) and (3) that include the phase transition width, the calculated values of the minimum reversible driving pressure can differ from the observed values for the same material. As shown in Fig. 3, it can be observed that the minimum reversible pressure of intermetallic compounds is larger compared to that of the other three categories. In formulae (2) and (3), both the phase transition width and thermal hysteresis are involved. Furthermore, we collected data on phase transition width and thermal hysteresis under atmospheric and applied pressure, as shown in Fig. 4. We found that phase transition widths and thermal hysteresis are distributed randomly within the range of 2 K to 20 K for most materials, without significant differences among the various material categories. As shown in Fig. 3, the minimum reversible pressure of intermetallic compounds is

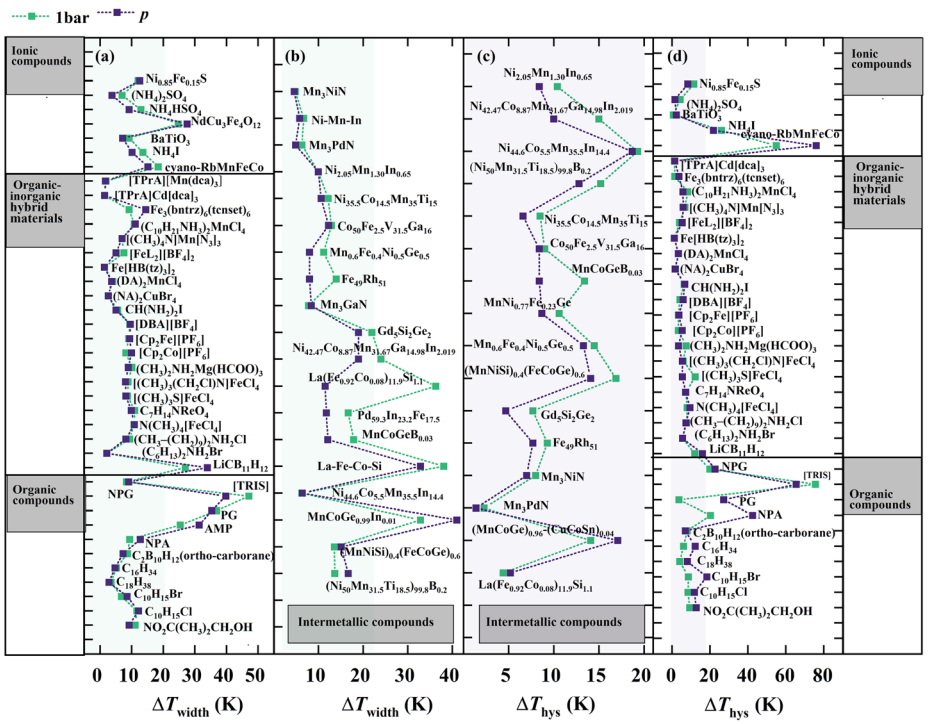

Fig. 4 The thermal hysteresis (ΔT_{hys}) and phase transition width (ΔT_{width}) under atmospheric pressure and hydrostatic pressure. (a) The phase transition widths of ionic compounds, organic–inorganic hybrid materials, and organic compounds. (b) The phase transition width of intermetallic compounds. (c) The thermal hysteresis of intermetallic compounds. (d) The thermal hysteresis of ionic compounds, organic–inorganic hybrid materials, and organic compounds. Green squares represent thermal hysteresis and phase transition width at atmospheric pressure, while purple squares represent thermal hysteresis and phase transition width under hydrostatic pressure. The dotted lines are a visual guide. Note: T_{width} values may vary depending on the measurement methodology and equipment used.

mainly distributed between 2 kbar and 10 kbar, while for the other three categories it is mainly distributed below 4 kbar. There is a clear difference in the distribution of minimum reversible pressure in the four categories. This indicates that most intermetallic compounds have a larger minimum reversible pressure, which shows a weak correlation with phase transition width and thermal hysteresis. The minimum reversible pressure of intermetallic compounds is relatively large, which may be attributed to the greater difficulty in compressing metal bonds than other types of chemical bonds (ionic bonds, hydrogen bonds, *etc.*). It should be noted that for specific materials, the phase transition width and thermal hysteresis can have a significant impact on the minimum reversible pressure. For instance, in organic compounds such as NPG and PG, the large thermal hysteresis and phase transition width result in a large minimum reversible pressure.

As key parameters for calculating the minimum reversible pressure, the behaviors of phase transition width and thermal hysteresis under hydrostatic pressure were investigated (refer to Tables 1 and 2 for detailed values). It was found that these parameters are not constant but rather vary with changes in pressure. The phase transition width and thermal hysteresis pertain to first-order phase transitions, which involve the mutual transformation between high-temperature and low-temperature phases induced by an external field. The phase transition width represents the interval in which high and low-temperature phases coexist and indicates the dynamic equilibrium between the two phases within a certain energy range. An extensive phase transition width suggests a low sensitivity of the high and low-temperature phases to temperature. Thermal hysteresis, on the other hand, reflects the symmetry discrepancy and thermal stability between the high and low-temperature phases.[76,160–163] The application of pressure can alter both thermal hysteresis and phase transition width, indicating that pressure can affect the thermal stability for high and low-temperature phases.

As shown in Fig. 4c, the purple line is always to the left of the green line, except for $(MnCoGe)_{0.96}$–$(CuCoSn)_{0.04}$ and $La(Fe_{0.92}Co_{0.08})_{11.9}Si_{1.1}$. This indicates that thermal hysteresis generally decreases with the application of pressure in intermetallic compounds. For some intermetallic compounds, the decrease in thermal hysteresis is significant. For example, the thermal hysteresis reduces to 33% of its original value for $Ni_{42.47}Co_{8.87}Mn_{31.67}Ga_{14.98}In_{2.019}$ and to 37% for $MnCoGeB_{0.03}$. Fig. 4b shows the change in phase transition width for intermetallic compounds under applied pressure. Under pressure, the phase transition width of intermetallic compounds generally decreases, and that of $La(Fe_{0.92}Co_{0.08})_{11.9}Si_{1.1}$ is notably reduced by 24.8 K, which may be related to the larger applied pressure (Table 1). For most intermetallic compounds, both thermal hysteresis and phase transition width decrease under pressure, indicating that shortening the interatomic distance can enhance their sensitivity to temperature. From Fig. 4a and d, it can be observed that thermal hysteresis and phase transition width do not exhibit a regular pattern under pressure. Overall, the phase transition width and thermal hysteresis of all materials change significantly under pressure, indicating that pressure influences the behavior of first-order phase transitions with respect to temperature.[164]

The refrigeration temperature range determines the potential application scenarios. A wider refrigeration temperature range often requires higher driving pressure and cost. Hence, it is important to balance economic feasibility and practicality. The goal of studies on the refrigeration temperature range is to apply the minimum operational pressure to achieve the maximum feasible temperature range. We calculated the pressure required for different materials to achieve a cooling of 60 K, which encompasses the standard temperature range required for daily refrigeration applications (approximately −20 °C to 40 °C), as shown in Fig. 5.

To determine the refrigeration temperature range, we first need to know that pressure can induce a phase transition from a large-volume phase to a small-volume phase by reducing the interatomic distance. However, a small-volume phase cannot revert to a large-volume phase regardless of the amount of pressure applied. This has been repeatedly verified in the BCE, where the inverse BCE results in a shift to lower temperatures, and the conventional BCE leads to a shift to higher temperatures under pressure. This is because the inverse BCE and conventional BCE originate from negative and positive thermal expansion, respectively. For the conventional BCE, the onset temperature of the phase transition from the LTP to the HTP marks the starting point (left end of the purple square in Fig. 5). For the inverse BCE, the temperature at which the phase transition from the HTP to the LTP is completed marks the starting point (right end of the green square in Fig. 5). The approximate

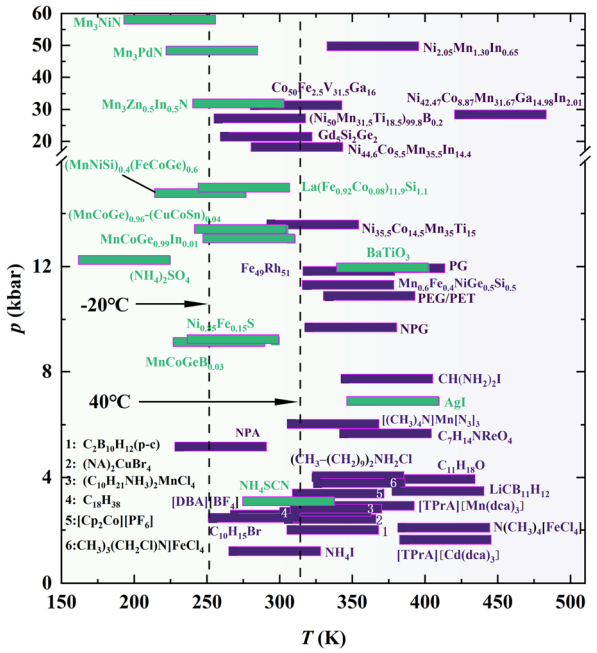

Fig. 5 The pressure required to extend the refrigeration temperature range by 60 K. The purple bars represent the conventional BCE, while the green bars correspond to the inverse BCE. The two dashed lines delineate the boundaries corresponding to the temperatures of −20 °C and 40 °C, respectively.

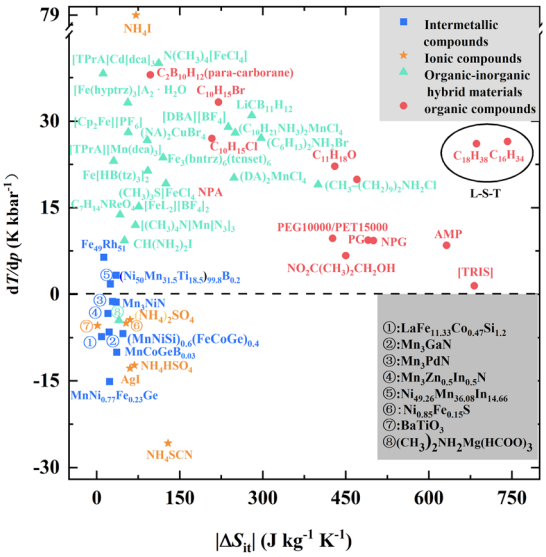

Fig. 6 Comparative analysis of the isothermal entropy change and dT/dp in giant and colossal barocaloric materials. The figure depicts a regular distribution of four categories of materials. The materials circled by the black hollow ellipse in the upper right of the figure indicate that their barocaloric effect originates from a liquid–solid phase transition. The barocaloric effect in other materials results from solid–solid phase transitions. The dashed line intersecting the ordinate at the zero point in the figure serves as a demarcation between conventional and inverse barocaloric effects. Regions above the dashed line correspond to the conventional BCE, while those below represent the inverse BCE.

phase transition temperatures during cooling for the inverse BCE and heating for the conventional BCE are considered as the starting points (the detailed values are listed in Tables 1 and 2). From these starting points, we extend the temperature range by 60 K towards higher temperatures for the conventional BCE and lower temperatures for the inverse BCE, respectively. The required pressure is calculated using the formula $p = p_{\min}^{\mathrm{rev}} + 60\ \mathrm{K}/(\mathrm{d}T/\mathrm{d}p)$, where $\mathrm{d}T/\mathrm{d}p = (\mathrm{d}T/\mathrm{d}p)_{\mathrm{c}}$ for the conventional BCE, and $\mathrm{d}T/\mathrm{d}p = (\mathrm{d}T/\mathrm{d}p)_{\mathrm{h}}$ for the inverse BCE, because the refrigeration temperature range of the material is of more concern. While acknowledging that excessive pressures can lead to material failure, we will, for the sake of simplicity, assume that the materials withstand the applied pressures without failure. It is found that for most intermetallic compounds, the pressure required to extend the refrigeration temperature range by 60 K exceeds 10 kbar. But organic–inorganic hybrid materials and organic compounds generally require smaller pressure.

The parameter dT/dp is crucial in determining the refrigeration temperature range. At a constant pressure, a greater value of dT/dp leads to a wider refrigeration temperature range. The isothermal entropy change, on the other hand, determines the caloric performance of materials. Fig. 6 illustrates the relationship between the isothermal entropy change and dT/dp to facilitate comparison of material performance. From Fig. 6, the four categories of barocaloric materials are distributed in a regular pattern. Intermetallic and ionic compounds are predominantly located in the lower left corner, indicating that they possess a relatively smaller isothermal entropy change and lower sensitivity to pressure. Hence, intermetallic and ionic compounds require larger pressure to induce the phase transition compared to the other two categories. Organic–inorganic hybrid materials are mainly distributed in the upper left area, indicating that they are generally sensitive to pressure and minimal pressure is required to induce the phase transition. Organic compounds are distributed along the diagonal line in Fig. 6, suggesting that they exhibit significant isothermal entropy changes and dT/dp. Additionally, solid–liquid phase transition materials (within the black oval frame in Fig. 6)

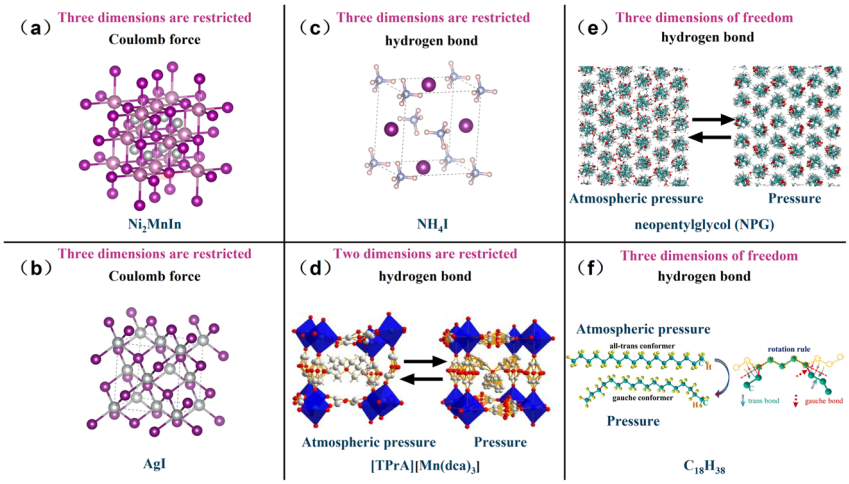

Fig. 7 Ball-and-stick models of the four categories of materials. (a) The structural model of the intermetallic compound Ni_2MnIn. (b) and (c) The structural model of ionic compounds AgI and NH_4I, respectively. (d) The structural model of [TPrA][Mn(dca)$_3$] in organic–inorganic hybrid materials. Reproduced from ref. 5 with permission from Springer Nature, copyright 2017. (e) and (f) are the structural models of organic compound $C_{18}H_{38}$ (Reproduced from ref. 29 with permission from Springer Nature, copyright 2022.) and NPG (Reproduced from ref. 16 with permission from Springer Nature, copyright 2019.), respectively. The red text above each structural model describes the constraints on spatial freedom experienced by the structure during phase transitions. The text in black font identifies the interactive forces within the crystal that must be counteracted by pressure during the phase transition process.

exhibit considerable isothermal entropy change and dT/dp values. From Fig. 6, it can be seen that there are large blank areas in the upper right and lower right corners of the graph. Future advancements in materials with superior barocaloric properties may occupy these regions.

Upon comparing the chemical compositions and structures of these materials, it is observed that most materials exhibiting large dT/dp and significant isothermal entropy change contain organic groups that participate in the phase transition. The order–disorder transition of these organic groups induces a substantial volume change, providing a large entropy change. Fig. 7 shows the crystal structures of typical materials in the four categories of materials. The degrees of freedom within the three-dimensional space of intermetallic and ionic compounds are restricted by metallic bonds or ionic bonds (Fig. 7a and b). In organic compounds and organic–inorganic hybrid materials, freedom extends to one or two dimensions, and even to all three dimensions. Consequently, their degrees of freedom are greater (twisting or freezing) during phase transitions, resulting in a larger entropy change. In intermetallic and ionic compounds, materials undergoing ferromagnetic and ferroelectric transitions exhibit a larger entropy change compared to those experiencing solely lattice transitions (see Section 2.1), primarily due to the additional degree of freedom associated with the magnetic moment or electric dipole moment in ferromagnetic and ferroelectric transitions.

A crystal exhibits a variety of interactive forces.[81,165,166] For analytical simplicity, this study considers only the primary forces that need to be resisted by pressure during phase transitions. As shown in, Ni_2MnIn (Fig. 7a) and AgI (Fig. 7b) are members of intermetallic and ionic compounds, respectively, and the atoms within these compounds are tightly bound in all three spatial dimensions by strong coulombic interactions. During the phase transition, the relative movement of atoms is constrained, which reduces the degree of freedom of the material. The interaction force in intermetallic and ionic compounds is a strong Coulomb interaction. Reducing the interatomic distances necessitates overcoming the coulombic interaction, thus necessitating a relatively higher pressure to facilitate the phase transition (see Fig. 3). Of course, there are some ion-molecular crystals (such as NH_4I and $(NH_4)_2SO_4$) in ionic compounds. The hydrogen atoms in ammonium ions are not subjected to strong coulombic forces.[132,167] In NH_4I, I^- and H of NH_4^+ form hydrogen bonds, and pressure impacts the weaker hydrogen bonds, prompting the reorientation of NH_4^+, thereby rendering the materials more pressure–sensitive (Fig. 7c).[63,168] In [TPrA][Mn(dca)$_3$], covalent bonds form a two-dimensional or three-dimensional network structure in the organic group, and the organic group is connected to another organic group through hydrogen bonds.[169–171] The organic groups are confined within two dimensions by covalent bonds (Fig. 7d), and the pressure mainly interacts with the hydrogen bonds in the crystal to stimulate the phase transition.

NPG is a molecular crystal. Organic molecules are interconnected *via* hydrogen bonds.[172] During phase transitions, the three dimensions of the molecule are not restricted by strong chemical bonds which endows the material with high degrees of freedom (Fig. 7e).[153] $C_{18}H_{38}$ is a small molecule organic material. Each molecular chain is linked to adjacent chains *via* hydrogen bonds. The molecular chains in $C_{18}H_{38}$ are free in three dimensions during phase transitions (Fig. 7f). According to the above analysis combined with experimental data (see Tables1 and 2), the requisite driving pressure in a barocaloric material primarily correlates with the force which plays a major role inside the material during phase transitions (Coulomb force or hydrogen bonds). The entropy change during the phase transition is predominantly associated with the material's degrees of freedom,[173,174] especially, the vibrational and rotational degrees of freedom.[85,175,176] In the case of three-dimensional restricted (Fig. 7a–c), rotational and vibrational degrees of freedom are suppressed, such as in intermetallic and ionic compounds, where there are vibrational, magnetic, or polarization degrees of freedom, but there are no particularly large differences in entropy changes among these materials (Fig. 6). In scenarios where spatial dimensions are unrestricted (Fig. 7d–f), molecules possess augmented vibrational and rotational degrees of freedom, and the isothermal entropy change of the material may increase significantly several times compared with that of other three-dimensionally restricted materials (Fig. 6). A higher degree of freedom within the material typically results in an enhanced entropy change.

Although hydrogen-bonded materials generally exhibit higher entropy changes compared to intermetallic and ionic compounds, the relationship between the number of hydrogen bonds and phase transition properties is complex. Specifically, as the number of hydrogen bonds increases from NPA to NPG to PG (which contain one, two, and three hydrogen bonds, respectively), the phase transition temperatures tend to increase and the dT/dP values decrease (Table 2). However, NPG, which contains two hydrogen bonds, exhibits the largest entropy change. This apparent contradiction can be attributed to the unique molecular structures and interactions present in each material. The balance between hydrogen bonds and other intermolecular forces, such as van der Waals interactions, can significantly influence the material's barocaloric properties. Therefore, while general trends can be observed, individual material characteristics and their specific intermolecular interactions must be considered to fully understand and predict barocaloric performance.

Beneath the dashed line in Fig. 6, there are intermetallic and ionic compounds, suggesting that these categories of materials demonstrate an inverse BCE. This phenomenon is attributed to the negative thermal expansion associated with magnetic and ferroelectric phase transitions, among others. In the conventional BCE, an increase in pressure leads to enhanced ordering within the material, consequently reducing entropy. Conversely, in inverse BCE scenarios, elevated pressure diminishes the material's order, culminating in an atypical increase in entropy.[177–179] As such, in the inverse BCE, materials are endothermic when pressure is applied and exothermic when pressure is released. This property of the inverse BCE enables the extension of its refrigeration temperature range to low or ultra-low temperatures, rendering it potentially advantageous for applications in low-temperature refrigeration.

Ultimately, we assess the two pivotal parameters in the BCE: the RC and the adiabatic temperature change (ΔT_{ad}). The values of RC and ΔT are obtained under the maximum pressure actually applied to the reported materials. The formula for calculating RC is RC = $|\Delta S_{it}| \times$ (FWHM of ΔS_{it}), where the FWHM denotes the full width at half maximum of the entropy as a function of temperature (for detailed RC information, refer to Tables 1 and 2). As depicted in Fig. 8, a comparative analysis of the cooling capacity and adiabatic temperature change is conducted across four categories of materials. Organic compounds and organic–inorganic hybrid materials exhibit larger cooling capacity and adiabatic temperature changes compared to the other two categories. Upon careful examination of the intermetallic and ionic compounds as shown in Fig. 8, it is observed that their cooling capacity values exhibit an approximately linear relationship with the adiabatic temperature change (Fig. 8b). This indicates that within intermetallic and ionic compounds, materials manifesting greater adiabatic temperature changes correspondingly exhibit enhanced cooling capacities, evidencing a robust correlation between these parameters. However, no such linear relationship exists between RC and $|\Delta T_{ad}|$ for organic–inorganic hybrid materials and organic compounds (Fig. 8a). Overall, the distribution of RC and $|\Delta T_{ad}|$ across all materials aligns diagonally, signifying that a substantial adiabatic temperature change typically implies a considerable refrigeration capacity.

During barocaloric cooling, thermal hysteresis directly affects the cooling performance and efficiency of the material. However, there is rarely a discussion on whether thermal hysteresis is due to the heat exchange process of the material or the intrinsic characteristics of its phase transition. Here, we have conducted a brief discussion on the relationship between thermal conductivity, intrinsic characteristics of phase transitions—volumetric change rate—and thermal hysteresis. We have collected the thermal conductivity data of some common materials,[180–189] as shown in Fig. 9b, and the corresponding thermal hysteresis of these materials is shown in Fig. 9a. Fig. 9b shows that the intrinsic thermal conductivity of intermetallic compounds is generally around 5 W m^{-1} K^{-1}, which is relatively high due to the large number of free electrons in intermetallic compounds. Organic–inorganic hybrid materials and organic materials generally have lower thermal conductivity, usually below 0.5 W m^{-1} K^{-1}, which is related to their weaker interaction forces, complex structures, and lack of effective energy transfer carriers. Most ionic compounds exhibit thermal conductivities exceeding 0.5 W m^{-1} K^{-1}, with some, such as for cyano-RbMnFeCo and $Ni_{0.85}Fe_{0.15}S$, surpassing those of intermetallic compounds by several times. In ionic compounds, thermal conduction is more complex. The stable lattice structure, cooperative ion migration, and polarity of ionic bonds facilitate the transfer of lattice vibration energy.

To determine whether hysteresis is caused by delayed heat transfer or the intrinsic characteristics of first-order phase transitions, we analyzed Fig. 9a, which shows that the thermal hysteresis of different materials generally ranges from 0–20 K. The distribution of thermal hysteresis in different materials

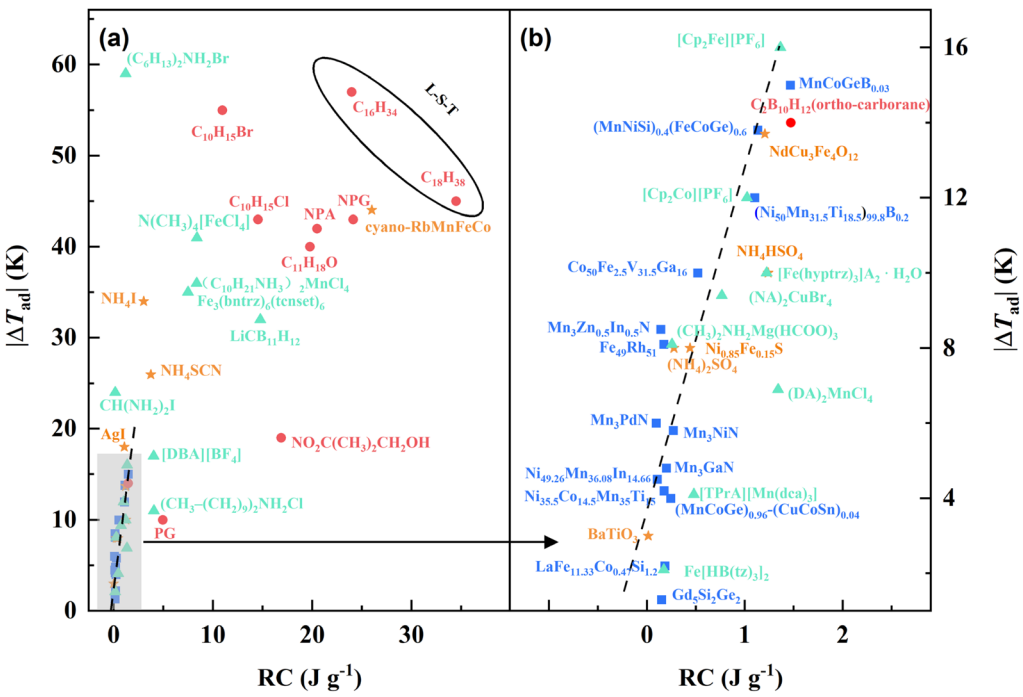

Fig. 8 Adiabatic temperature change as a function of RC. (a) The distribution of RC and the corresponding adiabatic temperature changes across all barocaloric materials. (b) A magnified view of the area within the grey box located in the lower left corner of (a). The blue squares (■) symbolize intermetallic compounds, while the orange pentagrams (★) denote ionic compounds. The green triangles (▲) represent organic–inorganic hybrid materials and the red circle (●) signifies organic compounds. The material outlined by the black hollow ellipse in the upper right corner of the figure suggests that its BCE originates from a liquid–solid phase transition. The dashed line denotes an approximate linear correlation between the adiabatic temperature change and RC for intermetallic and ionic compounds.

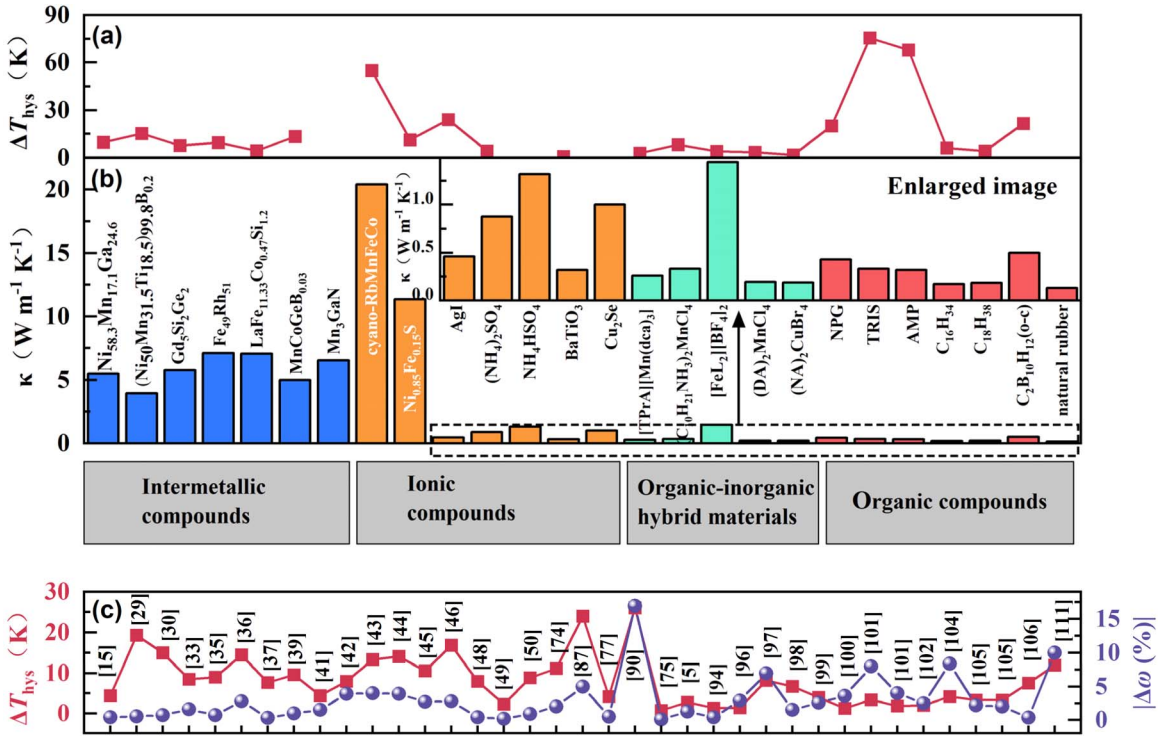

Fig. 9 The relationship between thermal hysteresis, thermal conductivity, and the volumetric change rate during first-order phase transitions. (a) The thermal hysteresis of the corresponding materials undergoing first-order phase transitions at atmospheric pressure shown in (b). (b) The thermal conductivity of the materials near their phase transition temperatures. The enlarged image of the low thermal conductivity within the dashed box is located in the top right corner. (c) The thermal hysteresis and volumetric change rate. The red curve represents the thermal hysteresis values under atmospheric pressure, while the blue curve represents the absolute values of the volumetric change rate at the first-order phase transition. The lines in the figures are visual guides. The numbers above the materials indicate their respective references.

does not show a clear trend compared to the distribution pattern of thermal conductivity, indicating that thermal hysteresis is not significantly related to thermal conductivity. However, when plotting the volumetric change rates associated with phase transitions and thermal hysteresis in Fig. 9c, we observed that, with the exception of a few materials, the trend of thermal hysteresis fluctuations is almost consistent with the volumetric change rates. This suggests that the thermal hysteresis of materials is related to their intrinsic volumetric change rate. However, in specific materials, it is important to note that the generation of thermal hysteresis is quite complex, requiring consideration of multiple factors, including the microstructure, thermal conduction mechanisms, environmental conditions, and phase transition dynamics.

4 Summary and outlook

This review comprehensively summarizes the barocaloric performances of reported materials, including intermetallic compounds, ionic compounds, organic–inorganic hybrid materials, and organic compounds. The distribution of barocaloric parameters across the four material categories exhibits pronounced regularity. Among the reported materials, organic–inorganic hybrid materials and organic compounds generally exhibit larger isothermal entropy changes and pressure sensitivity. Inferred from the reported data, barocaloric materials characterized by low driving pressure, significant entropy changes, and a wide refrigeration temperature range can be discovered in these two categories of materials in the future. Intermetallic and ionic compounds have smaller pressure sensitivity and isothermal entropy changes, but ferromagnetic and ferroelectric phase transitions in these two categories of materials cause their caloric effect to be controllable by multi-physical fields[190–196] and beneficial for cryogenic cooling due to the existence of the inverse BCE. These materials are anticipated to play a pivotal role in intelligent and micro-refrigeration systems, owing to their ferromagnetic and ferroelectric phase transitions. According to the regular pattern of barocaloric performance and the microstructure of materials during the phase transformation process, we concluded that the pressure sensitivity and isothermal entropy change of materials can be related to internal forces (Coulomb interaction or hydrogen bonds) and degrees of freedom (especially, the vibrational and rotational degrees of freedom) of the materials, respectively. This provides a new idea for the exploration of new materials with smaller driving pressure and larger isothermal entropy changes.

The magnitude of driving pressure is closely related to the internal forces within materials undergoing first-order phase transitions. The internal forces in these materials can be categorized into covalent bonds, metallic bonds, ionic bonds, hydrogen bonds, and van der Waals interactions, with their

strength generally decreasing in this order. Typically, materials with weaker internal forces, such as those with hydrogen bonds or van der Waals interactions, require lower driving pressures to induce phase transitions compared to materials with stronger covalent or metallic bonds. In designing barocaloric materials with easy pressure-driven phase transitions and large entropy changes, one should focus on materials with weaker internal forces. For instance, organic and organic–inorganic hybrid materials often require lower driving pressures due to the presence of hydrogen bonds and van der Waals interactions. Additionally, tuning the composition and structure to favor these weaker interactions can further enhance the material's barocaloric properties. Employing strategies such as incorporating flexible molecular chains or choosing hybrid compounds with organic cations can effectively achieve large entropy changes with manageable driving pressures.

Additionally, using computational simulations combined with machine learning to predict and design materials is also a very intriguing approach. Molecular dynamics simulations combined with machine learning have proven to be effective in simulating and predicting the performance of barocaloric materials with excellent properties, such as NH_4I,[167] and NPG.[154,197] Besides their application in molecular materials, machine learning, in combination with first-principles calculations, has been shown to be an effective tool for predicting key refrigeration parameters, heat effect changes, and material performance optimization strategies in framework materials such as $PbTiO_3$ (ref. 198) and LiI.[199]

In the future, the BCE could be further investigated and advanced in the following areas. Initially, compact centralized refrigeration technology will enhance the application of barocaloric refrigeration in electronic devices and various contexts.[200–202] Particularly, intermetallic and ionic compounds possess a relatively high density,[203] good thermal conductivity[50,156] and high strength, which are more advantageous for developing highly integrated and compact refrigeration devices. Second, the operational pressure within barocaloric materials ranges from tens to hundreds of MPa. Pressures of such magnitudes can be readily achieved by harnessing the interfacial stress[9,204] between materials and the design of the nano-microstructure of the material. The study of the BCE controlled by chemical stress and interfacial stress will be another important research field for the BCE,[205] and the application of high-pressure technology to materials could be realized through the control of microstructures and nano-scale self-assembly.[206–208] Ultimately, low or ultra-low temperature refrigeration might also be achievable with novel barocaloric materials exhibiting the inverse BCE.[209–211] We anticipate that this review will facilitate a comprehensive understanding and application of the BCE.

Data availability

No primary research results, software or code have been included and no new data were generated or analyzed as part of this review.

Author contributions

The draft of the manuscript was prepared by Y. S. and S. A. The manuscript was subsequently reviewed and guided by F. X. and C. W. All authors engaged in discussion and comment of the manuscript.

Conflicts of interest

The authors declare no competing financial interest.

Acknowledgements

This work was financially supported by the National Natural Science Foundation of China (52472273, 52272264, 52088101, and 92263202), the National Key Research and Development Program of China (2022YFA1402600 and 2021YFB3501202), Chinese-German Mobility programmed Project No. M-0273, and the Fundamental Research Funds for the Central Universities. We acknowledge Prof. Huilong Hou from Beihang University for fruitful discussion, and the facilities, and the scientific and technical assistance of the Analysis & Testing Center, Beihang University.

References

1 Programme, U. N. E., 2018, pp. 1–15, https://ozone.unep.org/node/3281.
2 X. Moya, S. Kar-Narayan and N. D. Mathur, *Nat. Mater.*, 2014, **13**, 439–450.
3 L. Manosa, A. Planes and M. Acet, *J. Mater. Chem. A*, 2013, **1**, 4925–4936.
4 L. Cirillo, A. Greco and C. Masselli, *Energies*, 2023, **16**, 6436.
5 J. M. Bermudez-Garcia, M. Sanchez-Andujar, S. Castro-Garcia, J. Lopez-Beceiro, R. Artiaga and M. A. Senaris-Rodriguez, *Nat. Commun.*, 2017, **8**, 1–8.
6 C. Aprea, A. Greco, A. Maiorino and C. Masselli, *Climate*, 2019, **7**, 1–14.
7 J. Liu, T. Gottschall, K. P. Skokov, J. D. Moore and O. Gutfleisch, *Nat. Mater.*, 2012, **11**, 1–7.
8 O. Tegus, E. B., K. H. J. Buschow and F. R. de Boer, *Nature*, 2002, **415**, 150–152.
9 Y. Liu, I. C. Infante, X. Lou, L. Bellaiche, J. F. Scott and B. Dkhil, *Adv. Mater.*, 2014, **26**, 6132–6137.
10 G. Zhang, X. Zhang, H. Huang, J. Wang, Q. Li, L. Q. Chen and Q. Wang, *Adv. Mater.*, 2016, **28**, 4811–4816.
11 B. Lu and J. Liu, *Sci. Bull.*, 2015, **60**, 1638–1643.
12 L. Manosa and A. Planes, *Philos. Trans. R. Soc., A*, 2016, **374**, 1–13.
13 D. Cong, W. Xiong, A. Planes, Y. Ren, L. Manosa, P. Cao, Z. Nie, X. Sun, Z. Yang, X. Hong and Y. Wang, *Phys. Rev. Lett.*, 2019, **122**, 255703.
14 E. Bonnot, R. Romero, L. Manosa, E. Vives and A. Planes, *Phys. Rev. Lett.*, 2008, **100**, 125901.
15 L. Manosa, D. Gonzalez-Alonso, A. Planes, E. Bonnot, M. Barrio, J.-L. Tamarit, S. Aksoy and M. Acet, *Nat. Mater.*, 2010, **9**, 478–481.

16 B. Li, Y. Kawakita, S. Ohira-Kawamura, T. Sugahara, H. Wang, J. Wang, Y. Chen, S. I. Kawaguchi, S. Kawaguchi, K. Ohara, K. Li, D. Yu, R. Mole, T. Hattori, T. Kikuchi, S.-i. Yano, Z. Zhang, Z. Zhang, W. Ren, S. Lin, O. Sakata, K. Nakajima and Z. Zhang, *Nature*, 2019, **567**, 506–510.
17 J. Garcia-Ben, I. Delgado-Ferreiro, J. Salgado-Beceiro and J. M. Bermudez-Garcia, *Materials*, 2021, **14**, 1–8.
18 J. Schipper, D. Bach, S. Moench, C. Molin, S. Gebhardt, J. Woellenstein, O. Schaefer-Welsen, C. Vogel, R. Langebach and K. Bartholome, *J. Phys.: Energy*, 2023, **5**, 045002.
19 P. Lloveras and J.-L. Tamarit, *Barocaloric Effects in theSolid State Materials and Methods*,2023. pp. 1–35.
20 L. Manosa, D. Gonzalez-Alonso, A. Planes, M. Barrio, J.-L. Tamarit, I. S. Titov, M. Acet, A. Bhattacharyya and S. Majumdar, *Nat. Commun.*, 2011, **2**, 595.
21 A. Aznar, P. Lloveras, M. Barrio, P. Negrier, A. Planes, L. Manosa, N. D. Mathur, X. Moya and J.-L. Tamarit, *J. Mater. Chem. A*, 2020, **8**, 639–647.
22 K. Alex Müller, F. Fauth, S. Fischer, M. Koch, A. Furrer and P. Lacorre, *Appl. Phys. Lett.*, 1998, **73**, 1056–1058.
23 T. Strassle and A. Furrer, *High Pressure Res.*, 2000, **17**, 325–333.
24 T. Strassle, A. Furrer, P. Lacorre and K. A. Muller, *J. Alloys Compd.*, 2000, **303**, 228–231.
25 T. Strassle, A. Furrer, F. Altorfer, K. Mattenberger, M. Bohm and H. Mutka, *J. Alloys Compd.*, 2001, **323**, 392–395.
26 T. Strassle, A. Furrer, A. Donni and T. Komatsubara, *J. Appl. Phys.*, 2002, **91**, 8543–8545.
27 M. S. Reis, *Coord. Chem. Rev.*, 2020, **417**, 213357.
28 K. Zhang, R. Song, J. Qi, Z. Zhang, Z. Zhang, C. Yu, K. Li, Z. Zhang and B. Li, *Adv. Funct. Mater.*, 2022, **32**, 2112622.
29 J. Lin, P. Tong, K. Zhang, K. Tao, W. Lu, X. Wang, X. Zhang, W. Song and Y. Sun, *Nat. Commun.*, 2022, **13**, 1–7.
30 S. P. Vallone, A. N. Tantillo, A. M. dos Santos, J. J. Molaison, R. Kulmaczewski, A. Chapoy, P. Ahmadi, M. A. Halcrow and K. G. Sandeman, *Adv. Mater.*, 2019, **31**, 1807334.
31 J. Li, M. Barrio, D. J. Dunstan, R. Dixey, X. Lou, J. L. Tamarit, A. E. Phillips and P. Lloveras, *Adv. Funct. Mater.*, 2021, **31**, 2105154.
32 E. Stern-Taulats, A. Planes, P. Lloveras, M. Barrio, J.-L. Tamarit, S. Pramanick, S. Majumdar, S. Yuce, B. Emre, C. Frontera and L. Manosa, *Acta Mater.*, 2015, **96**, 324–332.
33 X. He, S. Wei, Y. Kang, Y. Zhang, Y. Cao, K. Xu, Z. Li and C. Jing, *Scripta Mater.*, 2018, **145**, 58–61.
34 L. Manosa, E. Stern-Taulats, A. Planes, P. Lloveras, M. Barrio, J.-L. Tamarit, B. Emre, S. Yuce, S. Fabbrici and F. Albertini, *Phys. Status Solidi B*, 2014, **251**, 2114–2119.
35 X. J. He, K. Xu, S. X. Wei, Y. L. Zhang, Z. Li and C. Jing, *J. Mater. Sci.*, 2017, **52**, 2915–2923.
36 A. Aznar, A. Gracia-Conda, A. Planes, P. Lloveras, M. Barrio, J.-L. Tamarit, W. Xiong, D. Cong, C. Popescu and L. Manosa, *Phys. Rev. Mater.*, 2019, **3**, 044406.
37 Z. Wei, Y. Shen, Z. Zhang, J. Guo, B. Li, E. Liu, Z. Zhang and J. Liu, *Apl. Mater.*, 2020, **8**, 051101.
38 Y. Liu, Q. Shen, Z. Wei, W. Sun, F. Chen and J. Liu, *J. Appl. Phys.*, 2020, **127**, 055109.
39 H. Liu, Z. Li, Y. Zhang, Z. Ni, K. Xu and Y. Liu, *Scripta Mater.*, 2020, **177**, 1–5.
40 A. Taubel, T. Gottschall, M. Fries, T. Faske, K. P. Skokov and O. Gutfleisch, *J. Phys. D Appl. Phys.*, 2017, **50**, 113771.
41 S. Yuce, M. Barrio, B. Emre, E. Stern-Taulats, A. Planes, J.-L. Tamarit, Y. Mudryk, K. A. Gschneidner Jr, V. K. Pecharsky and L. Manosa, *Appl. Phys. Lett.*, 2012, **101**, 071906.
42 J.-D. Zou, *Chin. Phys. B*, 2012, **21**, 037503.
43 E. Stern-Taulats, A. Planes, P. Lloveras, M. Barrio, J.-L. Tamarit, S. Pramanick, S. Majumdar, C. Frontera and L. Manosa, *Phys. Rev. B:Condens. Matter Mater. Phys.*, 2014, **89**, 214105.
44 E. Stern-Taulats, A. Gracia-Condal, A. Planes, P. Lloveras, M. Barrio, J.-L. Tamarit, S. Pramanick, S. Majumdar and L. Manosa, *Appl. Phys. Lett.*, 2015, **107**, 152409.
45 J. Hao, F. Hu, J.-T. Wang, F.-R. Shen, Z. Yu, H. Zhou, H. Wu, Q. Huang, K. Qiao, J. Wang, J. He, L. He, J.-R. Sun and B. Shen, *Chem. Mater.*, 2020, **32**, 1807–1818.
46 R.-R. Wu, L.-F. Bao, F.-X. Hu, H. Wu, Q.-Z. Huang, J. Wang, X.-L. Dong, G.-N. Li, J.-R. Sun, F.-R. Shen, T.-Y. Zhao, X.-Q. Zheng, L.-C. Wang, Y. Liu, W.-L. Zuo, Y.-Y. Zhao, M. Zhang, X.-C. Wang, C.-Q. Jin, G.-H. Rao, X.-F. Han and B.-G. Shen, *Sci. Rep.*, 2015, **5**, 18027.
47 A. Aznar, P. Lloveras, J.-Y. Kim, E. Stern-Taulats, M. Barrio, J. Lluis Tamarit, C. F. Sanchez-Valdes, J. L. Sanchez Llamazares, N. D. Mathur and X. Moya, *Adv. Mater.*, 2019, **31**, 1903577.
48 Y. Kuang, X. Hao, Z. Zhang, B. Yang, B. Li, Z. Li, H. Yan, Y. Zhang, C. Esling, X. Zhao and L. Zuo, *J. Magn. Magn. Mater.*, 2022, **543**, 168639.
49 Q. Zeng, J. Shen, E. Liu, X. Xi, W. Wang, G. Wu and X. Zhang, *Chin. Phys. Lett.*, 2020, **37**, 076101.
50 P. Lloveras, T. Samanta, M. Barrio, I. Dubenko, N. Ali, J.-L. Tamarit and S. Stadler, *Apl. Mater.*, 2019, **7**, 061106.
51 D. Matsunami, A. Fujita, K. Takenaka and M. Kano, *Nat. Mater.*, 2015, **14**, 73–78.
52 D. Boldrin, E. Mendive-Tapia, J. Zemen, J. B. Staunton, T. Hansen, A. Aznar, J.-L. Tamarit, M. Barrio, P. Lloveras, J. Kim, X. Moya and L. F. Cohen, *Phys. Rev. X*, 2018, **8**, 041035.
53 K. Tao, W. Song, J. Lin, X. Zhang, P. Tong, Z. Zhang, J. Qi, B. Li, L. Ling, L. Ma and Y. Sun, *Scripta Mater.*, 2021, **203**, 114049.
54 D. Boldrin, E. Mendive-Tapia, J. Zemen, J. B. Staunton, A. M. Gomes, L. Ghivelder, J. Halpin, A. S. Gibbs, A. Aznar, J.-L. Tamarit, P. Lloveras, X. Moya and L. F. Cohen, *Phys. Rev. B*, 2021, **104**, 134101.
55 S. Singh, P. Kushwaha, F. Scheibel, H.-P. Liermann, S. R. Barman, M. Acet, C. Felser and D. Pandey, *Phys. Rev. B:Condens. Matter Mater. Phys.*, 2015, **92**, 020105(R).
56 Z. Yang, D. Y. Cong, X. M. Sun, Z. H. Nie and Y. D. Wang, *Acta Mater.*, 2017, **127**, 33–42.
57 M. Sasmaz, V. Koc and S. Guldal, *J. Supercond. Novel Magn.*, 2021, **34**, 2923–2931.

58 J. Lin, P. Tong, X. Zhang, Z. Wang, Z. Zhang, B. Li, G. Zhong, J. Chen, Y. Wu, H. Lu, L. He, B. Bai, L. Ling, W. Song, Z. Zhang and Y. Sun, *Mater. Horiz.*, 2020, **7**, 2690–2695.
59 A. Aznar, P. Lloveras, M. Romanini, M. Barrio, J.-L. Tamarit, C. Cazorla, D. Errandonea, N. D. Mathur, A. Planes, X. Moya and L. Manosa, *Nat. Commun.*, 2017, **8**, 1851.
60 P. Lloveras, E. Stern-Taulats, M. Barrio, J. L. Tamarit, S. Crossley, W. Li, V. Pomjakushin, A. Planes, L. Manosa, N. D. Mathur and X. Moya, *Nat. Commun.*, 2015, **6**, 8801.
61 M. V. Gorev, E. A. Mikhaleva, I. N. Flerov and E. V. Bogdanov, *J. Alloys Compd.*, 2019, **806**, 1047–1051.
62 E. A. Mikhaleva, I. N. Flerov, A. V. Kartashev, M. V. Gorev, E. V. Bogdanov and V. S. Bondarev, *Solid State Sci.*, 2017, **67**, 1–7.
63 Q. Ren, J. Qi, D. Yu, Z. Zhang, R. Song, W. Song, B. Yuan, T. Wang, W. Ren, Z. Zhang, X. Tong and B. Li, *Nat. Commun.*, 2022, **13**, 2293.
64 Y. Liu, J. Wei, P.-E. Janolin, I. C. Infante, X. Lou and B. Dkhil, *Appl. Phys. Lett.*, 2014, **104**, 162904.
65 E. Stern-Taulats, P. Lloveras, M. Barrio, E. Defay, M. Egilmez, A. Planes, J. L. Tamarit, L. Manosa, N. D. Mathur and X. Moya, *Apl. Mater.*, 2016, **4**, 091102.
66 Y. Kosugi, M. Goto, Z. Tan, A. Fujita, T. Saito, T. Kamiyama, W. T. Chen, Y. C. Chuang, H. S. Sheu, D. Kan and Y. Shimakawa, *Adv. Funct. Mater.*, 2021, **31**, 2009476.
67 Z. Zhang, K. Li, S. Lin, Z. Zhang and B. Li, *Sci. Adv.*, 2023, **9**, eadd0374.
68 Z. Zhang, X. Jiang, T. Hattori, X. Xu, M. Li, C. Yu, Z. Zhang, D. Yu, R. Mole, S.-i. Yano, J. Chen, L. He, C.-W. Wang, H. Wang, B. Li and Z. Zhang, *Mater. Horiz.*, 2023, **10**, 977–982.
69 S.-i. Ohkoshi, K. Nakagawa, M. Yoshikiyo, A. Namai, K. Imoto, Y. Nagane, F. Jia, O. Stefańczyk, H. Tokoro, J. Wang, T. Sugahara, K. Chiba, M. Kazuhiko, K. Isogai, K. Nishioka, T. Momiki and R. Hatano, *Nat. Commun.*, 2023, **14**, 8466.
70 J. Manuel Bermudez-Garcia, S. Yanez-Vilar, A. Garcia-Fernandez, M. Sanchez-Andujar, S. Castro-Garcia, J. Lopez-Beceiro, R. Artiaga, M. Dilshad, X. Moya and M. Antonia Senaris-Rodriguez, *J. Mater. Chem. C*, 2018, **6**, 9867–9874.
71 P. J. von Ranke, B. P. Alho, R. M. Ribas, E. P. Nobrega, A. Caldas, V. S. R. de Sousa, M. V. Colaco, L. F. Marques, D. L. Rocco and P. O. Ribeiro, *Phys. Rev. B*, 2018, **98**, 224408.
72 M. Romanini, Y. Wang, K. Gurpinar, G. Ornelas, P. Lloveras, Y. Zhang, W. Zheng, M. Barrio, A. Aznar, A. Gracia-Condal, B. Emre, O. Atakol, C. Popescu, H. Zhang, Y. Long, L. Balicas, J. Lluis Tamarit, A. Planes, M. Shatruk and L. Manosa, *Adv. Mater.*, 2021, **33**, 2008076.
73 J. Salgado-Beceiro, A. Nonato, R. X. Silva, A. García-Fernández, M. Sánchez-Andújar, S. Castro-García, E. Stern-Taulats, M. A. Señarís-Rodríguez, X. Moya and J. M. Bermúdez-García, *Mater. Adv.*, 2020, **1**, 3167–3170.
74 J. Seo, J. D. Braun, V. M. Dev and J. A. Mason, *J. Am. Chem. Soc.*, 2022, **144**, 6493–6503.
75 J. Seo, R. D. McGillicuddy, A. H. Slavney, S. Zhang, R. Ukani, A. A. Yakovenko, S.-L. Zheng and J. A. Mason, *Nat. Commun.*, 2022, **13**, 2536.
76 M. Seredyuk, R. Li, K. Znovjyak, Z. Zhang, F. J. Valverde-Munoz, B. Li, M. C. Munoz, Q. Li, B. Liu, G. Levchenko and J. A. Real, *Adv. Funct. Mater.*, 2024, 2315487.
77 C. Yu, J. Huang, J. Qi, P. Liu, D. Li, T. Yang, Z. Zhang and B. Li, *Apl. Mater.*, 2022, **10**, 011109.
78 J. García-Ben, J. M. Bermúdez-García, R. J. C. Dixey, I. Delgado-Ferreiro, A. L. Llamas-Saiz, J. López-Beceiro, R. Artiaga, A. García-Fernández, U. B. Cappel, B. Alonso, S. Castro-García, A. E. Phillips, M. Sánchez-Andújar and M. A. Señarís-Rodríguez, *J. Mater. Chem. A*, 2023, **11**, 22232–22247.
79 J. Garcia-Ben, I. Delgado-Ferreiro, R. J. C. Dixey, S. Castro-Garcia, J. Lopez-Beceiro, R. Artiaga, M. Sanchez-Andujar, A. E. Phillips, J. M. Bermudez-Garcia and M. A. Senaris-Rodriguez, *J. Mater. Chem. A*, 2024, **12**, 23751–23760.
80 M. Szafrański, W.-J. Wei, Z.-M. Wang, W. Li and A. Katrusiak, *APL Mater.*, 2018, **6**, 100701.
81 J. Salgado-Beceiro, J. M. Bermudez-Garcia, E. Stern-Taulats, J. Garcia-Ben, S. Castro-Garcia, M. Sanchez-Andujar, X. Moya & M. A. Senaris-Rodriguez, *ChemRxiv*, 2021. DOI: 10.26434/chemrxiv-2021-c4hx5.
82 A. Salvatori, D. Aguila, G. Aromi, L. Manosa, A. Planes, P. Lloveras, L. C. Pardo, M. Appel, G. F. Nataf, F. Giovannelli, M. Barrio, J. L. Tamarit and M. Romanini, *J. Mater. Chem. A*, 2023, **11**, 12140–12150.
83 Y.-H. Gao, D.-H. Wang, F.-X. Hu, Q.-Z. Huang, Y.-T. Song, S.-K. Yuan, Z.-Y. Tian, B.-J. Wang, Z.-B. Yu, H.-B. Zhou, Y. Kan, Y. Lin, J. Wang, Y.-l. Li, Y. Liu, Y.-Z. Chen, J.-R. Sun, T.-Y. Zhao and B.-G. Shen, *Nat. Commun.*, 2024, **15**, 1838.
84 J. Seo, R. Ukani, J. Zheng, J. D. Braun, S. Wang, F. E. Chen, H. K. Kim, S. Zhang, C. Thai, R. D. McGillicuddy, H. Yan, J. J. Vlassak and J. A. Mason, *J. Am. Chem. Soc.*, 2024, **146**, 2736–2747.
85 M. Zeng, C. Escorihuela-Sayalero, T. Ikeshoji, S. Takagi, S. Kim, S.-i. Orimo, M. Barrio, J.-L. Tamarit, P. Lloveras, C. Cazorla and K. Sau, *Adv. Sci.*, 2024, 2306488.
86 M. Gelpi, J. Garcia-Ben, S. Rodriguez-Hermida, J. Lopez-Beceiro, R. Artiaga, A. Baalina, M. Romero-Gomez, J. Romero-Gomez, S. Zaragoza, J. Salgado-Beceiro, J. Walker, C. J. McMonagle, S. Castro-Garcia, M. Sanchez-Andujar, M. A. Senaris-Rodriguez and J. M. Bermudez-Garcia, *Adv. Mater.*, 2024, **36**, 2310499.
87 J. Garcia-Ben, J. Lopez-Beceiro, R. Artiaga, J. Salgado-Beceiro, I. Delgado-Ferreiro, Y. V. Kolen'ko, S. Castro-Garcia, M. Antonia Senaris-Rodriguez, M. Sanchez-Andujar and J. Manuel Bermudez-Garcia, *Chem. Mater.*, 2022, **34**, 3323–3332.
88 P. Lloveras, A. Aznar, M. Barrio, P. Negrier, C. Popescu, A. Planes, L. Manosa, E. Stern-Taulats, A. Avramenko, N. D. Mathur, X. Moya and J. L. Tamarit, *Nat. Commun.*, 2019, **10**, 1803.
89 A. Aznar, P. Negrier, A. Planes, L. Manosa, E. Stern-Taulats, X. Moya, M. Barrio, J.-L. Tamarit and P. Lloveras, *Appl. Mater. Today*, 2021, **23**, 101023.
90 Z. Yu, H. Zhou, F. Hu, C. Liu, S. Yuan, D. Wang, J. Hao, Y. Gao, Y. Wang, B. Wang, Z. Tian, Y. Lin, C. Zhang,

Z. Yin, J. Wang, Y. Chen, Y. Li, J. Sun, T. Zhao and B. Shen, *NPG Asia Mater.*, 2022, **14**, 96.
91 A. Salvatori, P. Negrier, A. Aznar, M. Barrio, J. L. Tamarit and P. Lloveras, *Apl. Mater.*, 2022, **10**, 111117.
92 A. Salvatori, M. Barrio, P. Negrier, S. Massip, M. Romanini, A. Aznar, P. Lloveras and J.-L. Tamarit, *J. Phys.: Energy*, 2023, **5**, 045015.
93 T. Xiong, J. Lin, T. Zhou, G. Shi, T. Ye, X. Pan, K. Liu, R. Jiang, R. Zhang, W. Song, P. Tong and Y. Sun, *Appl. Phys. Lett.*, 2024, 125.
94 A. N. Khan, L. M. Moreno-Ramirez, A. Diaz-Garcia, J. Yan Law and V. Franco, *J. Alloys Compd.*, 2023, **931**, 167559.
95 V. K. Sharma and M. Manekar, *J. Magn. Magn. Mater.*, 2023, **565**, 170236.
96 T. Samanta, P. Lloveras, A. U. Saleheen, D. L. Lepkowski, E. Kramer, I. Dubenko, P. W. Adams, D. P. Young, M. Barrio, J. L. Tamarit, N. Ali and S. Stadler, *Appl. Phys. Lett.*, 2018, **112**, 021907.
97 Y. Kuang, J. Qi, H. Xu, B. Yang, B. Li, Z. Li, H. Yan, Y. Zhang, C. Esling, X. Zhao and L. Zuo, *Scripta Mater.*, 2021, **200**, 113908.
98 K. W. Shi, Y. Sun, J. Yan, S. H. Deng, L. Wang, H. Wu, P. W. Hu, H. Q. Lu, M. I. Malik, Q. Z. Huang and C. Wang, *Adv. Mater.*, 2016, **28**, 3761–3767.
99 A. Fujita and K. Takenaka, *J. Phys.:Conf. Ser.*, 2017, **868**, 012004.
100 E. Mendive-Tapia and J. B. Staunton, *Phys. Rev. B*, 2019, **99**, 144424.
101 L. G. de Medeiros Jr, N. A. de Oliveira and A. Troper, *J. Appl. Phys.*, 2008, **103**, 113909.
102 Y. Liu, X. Zheng, F. Liang, F. Hu, Q. Huang, Z. Li and J. Liu, *NPG Asia Mater.*, 2022, **14**, 30.
103 E. Mendive Tapia, C. E. Patrick, T. Hickel, J. Neugebauer and J. B. Staunton, *J. Phys.: Energy*, 2023, **5**, 034004.
104 T. S. T. Alvaranega, B. P. Alho, E. P. Nobrega, P. O. Ribeiro, A. Caldas, V. S. R. de Sousa, A. Magnus, G. Carvalho, N. A. de Oliveira and P. J. von Ranke, *J. Appl. Phys.*, 2014, **116**, 243908.
105 N. A. Zarkevich and D. D. Johnson, *J. Alloys Compd.*, 2019, **802**, 712–722.
106 R. Greeshma and R. Banerjee, *Pramana - J. Phys.*, 2023, **97**, 95.
107 N. A. de Oliveira, *J. Phys-Condens.Mat.*, 2008, **20**, 175209.
108 E. J. R. Plaza and J. C. P. Campoy, *Phys. Rev. B:Condens. Matter Mater. Phys.*, 2007, **75**, 174419.
109 L. G. de Medeiros Jr, N. A. de Oliveira and A. Troper, *J. Magn. Magn. Mater.*, 2010, **322**, 1558–1560.
110 R. Huang, Y. Liu, W. Fan, J. Tan, F. Xiao, L. Qian and L. Li, *J. Am. Chem. Soc.*, 2013, **135**, 11469–11472.
111 N. A. de Oliveira, *J. Appl. Phys.*, 2013, **113**, 033910.
112 E. A. Mikhaleva, I. N. Flerov, V. S. Bondarev, M. V. Gorev, A. D. Vasiliev and T. N. Davydova, *Ferroelectrics*, 2012, **430**, 78–83.
113 E. A. Mikhaleva, I. N. Flerov, M. V. Gorev, M. S. Molokeev, A. V. Cherepakhin, A. V. Kartashev, N. V. Mikhashenok and K. A. Sablina, *Phys. Solid State*, 2012, **54**, 1832–1840.
114 S. Patel, A. Chauhan, R. Vaish and P. Thomas, *Appl. Phys. Lett.*, 2016, **108**, 072903.
115 X. Kang, R. Ishikawa, A. A. Belik, Y. Tsujimoto, M. Arai, S. Kawata and K. Yamaura, *Inorg. Chem.*, 2023, **62**, 18474–18484.
116 Y. Shi, Y. Guo, X. Wang, A. J. Princep, D. Khalyavin, P. Manuel, Y. Michiue, A. Sato, K. Tsuda, S. Yu, M. Arai, Y. Shirako, M. Akaogi, N. Wang, K. Yamaura and A. T. Boothroyd, *Nat. Mater.*, 2013, **12**, 1024–1027.
117 A. V. Kartashev, E. A. Mikhaleva, M. V. Gorev, E. V. Bogdanov, A. V. Cherepakhin, K. A. Sablina, N. V. Mikhashonok, I. N. Flerov and N. V. Volkov, *J. Appl. Phys.*, 2013, **113**, 073901.
118 S. Patel, A. Chauhan, R. Vaish and C. S. Lynch, *J. Am. Ceram. Soc.*, 2017, **100**, 4902–4911.
119 Y. Kosugi, M. Goto, Z. Tan, D. Kan, M. Isobe, K. Yoshii, M. Mizumaki, A. Fujita, H. Takagi and Y. Shimakawa, *Sci. Rep.*, 2021, **11**, 12682.
120 J. Min, A. K. Sagotra and C. Cazorla, *Phys. Rev. Mater.*, 2020, **4**, 015403.
121 A. Corrales-Salazar, R. T. Brierley, P. B. Littlewood and G. G. Guzman-Verri, *Phys. Rev. Mater.*, 2017, **1**, 053601.
122 M. V. Gorev, I. N. Flerov, E. V. Bogdanov, V. N. Voronov and N. M. Laptash, *Phys. Solid State*, 2010, **52**, 377–383.
123 I. N. Flerov, M. V. Gorev, V. D. Fokina, A. F. Bovina, E. V. Bogdanov, E. I. Pogoreltsev and N. M. Laptash, *J. Fluorine. Chem.*, 2011, **132**, 713–718.
124 I. N. Flerov, A. V. Kartashev, M. V. Gorev, E. V. Bogdanov, S. V. Mel'nikova, M. S. Molokeev, E. I. Pogoreltsev and N. M. Laptash, *J. Fluorine Chem.*, 2016, **183**, 1–9.
125 M. Gorev, E. Bogdanov, I. Flerov and N. Laptash, *J. Phys.:Condens. Matter*, 2010, **22**, 185901.
126 M. V. Gorev, E. V. Bogdanov and I. N. Flerov, *Scripta Mater.*, 2017, **139**, 53–57.
127 M. V. Gorev, E. V. Bogdanov and I. N. Flerov, *J. Phys. D Appl. Phys.*, 2017, **50**, 1–16.
128 M. V. Gorev, E. V. Bogdanov, I. N. Flerov, A. G. Kocharova and N. M. Laptash, *Phys. Solid State*, 2010, **52**, 167–175.
129 I. N. Flerov, M. V. Gorev, A. V. Kartashev, E. I. Pogorel'tsev and N. M. Laptash, *J. Mater. Sci.*, 2019, **54**, 14287–14295.
130 E. A. Mikhaleva, I. N. Flerov, M. V. Gorev, V. S. Bondarev and E. V. Bogdanov, *Crystals*, 2020, **10**, 51.
131 E. Mikhaleva, M. Gorev, V. Bondarev, E. Bogdanov and I. Flerov, *Scripta Mater.*, 2021, **191**, 149–154.
132 B. E. Meijer, G. Cai, F. Demmel, H. C. Walker and A. E. Phillips, *Phys. Rev. B*, 2022, **106**, 064302.
133 J. M. Bermudez-Garcia, M. Sanchez-Andujar and M. A. Senaris-Rodriguez, *J. Phys. Chem. Lett.*, 2017, **8**, 4419–4423.
134 P. J. von Ranke, B. P. Alho, P. H. S. da Silva, R. M. Ribas, E. P. Nobrega, V. S. R. de Sousa, A. M. G. Carvalho and P. O. Ribeiro, *Phys. Status Solidi B*, 2021, **258**, 2100108.
135 Y. Gao, H. Liu, F. Hu, H. Song, H. Zhang, J. Hao, X. Liu, Z. Yu, F. Shen, Y. Wang, H. Zhou, B. Wang, Z. Tian, Y. Lin, C. Zhang, Z. Yin, J. Wang, Y. Chen, Y. Li, Y. Song, Y. Shi, T. Zhao, J. Sun, Q. Huang and B. Shen, *NPG Asia Mater.*, 2022, **14**, 34.

136 M. Maczka, A. Gagor, M. Ptak, D. Stefanska, L. Macalik, A. Pikul and A. Sieradzki, *Dalton Trans.*, 2019, **48**, 13006–13016.
137 M. G. Basavarajappa, M. K. Nazeeruddin and S. Chakraborty, *Appl. Phys. Rev.*, 2021, **8**, 041309.
138 J. Garcia-Ben, L. N. McHugh, T. D. Bennett and J. M. Bermudez-Garcia, *Coord. Chem. Rev.*, 2022, **454**, 214337.
139 P. J. von Ranke, B. P. Alho and P. O. Ribeiro, *J. Alloys Compd.*, 2018, **749**, 556–560.
140 P. J. von Ranke, B. P. Alho, E. P. Nobrega, A. Caldas, V. S. R. de Sousa, M. V. Colaco, L. F. Marques, G. M. Rocha, D. L. Rocco and P. O. Ribeiro, *J. Magn. Magn. Mater.*, 2019, **489**, 165421.
141 Z. Xie, G. Sebald and D. Guyomar, *Appl. Therm. Eng.*, 2017, **111**, 914–926.
142 N. Weerasekera, K. P. K. Ajjarapu, K. Sudan, G. Sumanasekera, K. Kate and B. Bhatia, *Front. Energy Res.*, 2022, **10**, 887006.
143 N. M. Bom, W. Imamura, E. O. Usuda, L. S. Paixao and A. M. G. Carvalho, *Macro Lett.*, 2018, **7**, 31–36.
144 C. M. Miliante, A. M. Christmann, E. O. Usuda, W. Imamura, L. S. Paixao, A. M. G. Carvalho and A. R. Muniz, *Macromolecules*, 2020, **53**, 2606–2615.
145 A. M. G. Carvalho, W. Imamura, E. O. Usuda and N. M. Bom, *Eur. Polym. J.*, 2018, **99**, 212–221.
146 W. Imamura, E. O. Usuda, L. S. Paixao, N. Molina Bom, A. M. Gomes and A. M. Gomes Carvalho, *Chin. J. Polym. Sci.*, 2020, **38**, 999–1005.
147 N. M. Bom, E. O. Usuda, M. da Silva Gigliotti, D. J. M. de Aguiar, W. Imamura, L. S. Paixao and A. M. G. Carvalho, *Chin. J. Polym. Sci.*, 2020, **38**, 769–775.
148 C. M. Miliante, A. M. Christmann, R. P. Soares, J. R. Bocca, C. S. Alves, A. M. G. Carvalho and A. R. Muniz, *J. Mater. Chem. A*, 2022, **10**, 8344–8355.
149 C. Zhang, D. Wang, S. Qian, Z. Zhang, X. Liang, L. Wu, L. Long, H. Shi and Z. Han, *Mater. Horiz.*, 2022, **9**, 1293.
150 C. Aprea, A. Greco, A. Maiorino and C. Masselli, *Energies*, 2019, **12**, 2902.
151 X. Su, Z. Zhang, J. Liu, Q. Zheng, Z. Li, J. Shen, B. Li and J. Du, *J. Phys. Chem. Lett.*, 2024, **15**, 1962–1968.
152 Y. Qian, D.-S. Shao, W.-W. Yao, N. Wan, X.-Z. Wang and X.-M. Ren, *J. Phys. Chem. C*, 2020, **124**, 20722–20729.
153 F. B. Li, M. Li, X. Xu, Z. C. Yang, H. Xu, C. K. Jia, K. Li, J. He, B. Li and H. Wang, *Nat. Commun.*, 2020, **11**, 4190.
154 F. Li, C. Niu, X. Xu, M. Li and H. Wang, *Appl. Phys. Lett.*, 2022, **121**, 223902.
155 Z. Dai, B. Shao, Q. Chen, Y. Ding, Y. Li, M. Zhang, E. Yin, X. She, X. Zhang and D. Zhao, *Adv. Funct. Mater.*, 2023, 2307822.
156 Y. Liu, H. Zhou, Z. Xu, D. Liu, J. Li, F. Hu and T. Ma, *Mater. Res. Lett.*, 2022, **10**, 675–681.
157 P. A. Domanski, J. Steven Brown, J. Heo, J. Wojtusiak and M. O. McLinden, *Int. J. Refrig.*, 2014, **38**, 71–79.
158 M. Masche, L. Ianniciello, J. Tušek and K. Engelbrecht, *Int. J. Refrig.*, 2021, **121**, 302–312.
159 Y. Duan, S. Semin, P. Tinnemans, J. Xu and T. Rasing, *Small*, 2021, **17**, 2006757.
160 M. A. Carpenter, M. B. Costa, G. F. Nataf and X. Moya, *Phys. Rev. Mater.*, 2023, **7**, 083601.
161 D. Kim, H. Kim, E. Lee, K. S. Jin and J. Yoon, *Chem. Mater.*, 2016, **28**, 8807–8814.
162 S.-i. O. Hiroko Tokoro, T. Matsuda and K. Hashimoto, *Inorg. Chem.*, 2003, **43**, 5231–5236.
163 M. Ren, J. H. L, Y. Dong, L. Q. Yang and M. Z. Su, *Chem. Mater.*, 1999, **11**, 1576–1580.
164 S. Wang, H. Fan, Z. Zhang, L. Sun, J. Chen, N. Yang, Y. Zhou, B. Li and L. Dai, *J. Mater. Chem. C*, 2022, **10**, 14431–14438.
165 L. M. Malec, M. Z. Brela and K. M. Stadnicka, *Acta Mater.*, 2021, **209**, 116782.
166 F. Li, M. Li, C. Niu and H. Wang, *Appl. Phys. Lett.*, 2022, **120**, 073902.
167 X. Xu, F. Li, C. Niu, M. Li and H. Wang, *Appl. Phys. Lett.*, 2023, **122**, 043901.
168 S. Yuan, B. E. Meijer, G. Cai, R. J. C. Dixey, F. Demmel, M. T. Dove, J. Liu, H. Y. Playford, H. C. Walker and A. E. Phillips, *Adv. Funct. Mater.*, 2022, **32**, 1–12.
169 L.-J. Ji, S.-J. Sun, Y. Qin, K. Li and W. Li, *Coord. Chem. Rev.*, 2019, **391**, 15–29.
170 R.-X. Li, L. Zhou, P.-P. Shi, X. Zheng, J.-X. Gao, Q. Ye and D.-W. Fu, *New J. Chem.*, 2019, **43**, 154–161.
171 R. X. Silva, R. R. Hora, A. Nonato, A. Garcia-Fernandez, J. Salgado-Beceiro, M. Antonia Senaris-Rodriguez, M. Sanchez Andujar, A. P. Ayala and C. W. A. Paschoal, *Spectrochim. Acta, Part A*, 2023, **289**, 122198.
172 N. A. de Oliveira, *Acta Mater.*, 2023, **246**, 118657.
173 D. Boldrin, *Appl. Phys. Lett.*, 2021, **118**, 170502.
174 Y. Shimakawa and Y. Kosugi, *J. Mater. Chem. A*, 2023, **11**, 12695–12702.
175 C. Escorihuela-Sayalero, L. C. Pardo, M. Romanini, N. Obrecht, S. Loehle, P. Lloveras, J.-L. Tamarit and C. Cazorla, *npj Comput. Mater.*, 2024, **10**, 1–10.
176 C. Niu, F. Li, X. Xu, W. Xie, G. Zhai, M. Li and H. Wang, *Appl. Phys. Lett.*, 2024, **124**, 103905.
177 Y. Song, Q. Sun, M. Xu, J. Zhang, Y. Hao, Y. Qiao, S. Zhang, Q. Huang, X. Xing and J. Chen, *Mater. Horiz.*, 2020, **7**, 275–281.
178 R. P. Santana, N. A. de Oliveira and P. J. von Ranke, *J. Phys.:Condens. Matter*, 2011, **23**, 306003.
179 K. Takenaka, T. Sugiura, Y. Kadowaki, M. Ozeki, Y. Okamoto and A. Fujita, *J. Phys. Soc. Jpn.*, 2021, **90**, 044601.
180 Y. C. Zhang, V. Franco, H. X. Peng and F. X. Qin, *Scripta Mater.*, 2021, **201**, 113956.
181 S. Fujieda, Y. H. a, A. Fujita and K. Fukamichi, *J. Appl. Phys.*, 2003, **95**, 2429–2431.
182 K. Nishikawa, Y. Takeda and T. Motohiro, *Appl. Phys. Lett.*, 2013, 102.
183 Y.-Y. Che, J. Shen, J.-C. Zhou and C.-H. He, *J. Chem. Eng. Data*, 2012, **57**, 1486–1491.
184 N. Hoshino and T. Akutagawa, *J. Chem. Phys.*, 2020, **153**, 194503.

185 B. K. Shaw, A. R. Hughes, M. Ducamp, S. Moss, A. Debnath, A. F. Sapnik, M. F. Thorne, L. N. McHugh, A. Pugliese, D. S. Keeble, P. Chater, J. M. Bermudez-Garcia, X. Moya, S. K. Saha, D. A. Keen, F.-X. Coudert, F. Blanc and T. D. Bennett, *Nat. Chem.*, 2021, **13**, 778–785.
186 X. Wang, Q. Guo, Y. Zhong, X. Wei and L. Liu, *Renewable Energy*, 2013, **51**, 241–246.
187 Z. Y. Zhang and Y. P. Xu, *Sol. Energy*, 2001, **71**, 299–303.
188 C. Vélez, M. Khayet and J. M. Ortiz de Zárate, *Appl. Energy*, 2015, **143**, 383–394.
189 Y. A. N. He and Y. Tang, *J. Theor. Comput. Chem.*, 2013, **12**, 1350011.
190 Y. Vysochanskii and O. Derzhko, *Condens. Matter Phys.*, 2022, **25**, 43711.
191 J.-W. G. Bos, C. V. Colin and T. T. M. Palstra, *Phys. Rev. B:Condens. Matter Mater. Phys.*, 2008, **78**, 094416.
192 A. Czernuszewicz, J. Kaleta and D. Lewandowski, *Energy Convers. Manag.*, 2018, **178**, 335–342.
193 S. Faehler and V. K. Pecharsky, *Mrs Bulletin*, 2018, **43**, 264–268.
194 A. U. Saleheen, *The Effects of Pressure and Magnetic Field on Phase Transitions and Related Physical Properties in Solid State Caloric Materials*, doctoral thesis, 2018.
195 D. Clifford, V. Sharma, K. Deepak, R. V. Ramanujan and R. Barua, *IEEE Trans. Magn.*, 2021, **57**, 2500405.
196 L. Manosa, E. Stern-Taulats, A. Gracia-Condal and A. Planes, *J. Phys.: Energy*, 2023, **5**, 024016.
197 F. Li, C. Niu, X. Xu, W. Xie, M. Li and H. Wang, *Appl. Phys. Lett.*, 2022, **121**, 223902.
198 X. Xu, W. Xie, F. Li, C. Niu, M. Li and H. Wang, *Phys. Rev. Appl.*, 2024, **22**, 014036.
199 Y. Dai and M. Wu, *Adv. Phys. Res.*, 2024, **2751–1200**, 2400125.
200 A. Shakouri and Z. Yan, *IEEE Trans. Compon., Packag. Technol.*, 2005, **28**, 65–69.
201 H. Cui, Q. Zhang, Y. Bo, P. Bai, M. Wang, C. Zhang, X. Qian and R. Ma, *Joule*, 2022, **6**, 258–268.
202 Q. Zhang, K. Deng, L. Wilkens, H. Reith and K. Nielsch, *Nat. Electron.*, 2022, **5**, 333–347.
203 L. Manosa and A. Planes, *Adv. Mater.*, 2017, **29**, 1603607.
204 Y.-K. Wang, Q.-L. Zhao, J.-J. Di, G.-P. He, L. Zhao, T.-T. Su, M.-Y. Zhang, J. Zhang, X. Liang and D. Bu, *Phys. Status Solidi A*, 2021, **218**, 2000651.
205 K. Lin, Q. Li, R. Yu, J. Chen, J. P. Attfield and X. Xing, *Chem. Soc. Rev.*, 2022, **51**, 5351–5364.
206 R. A. Hughes, E. Menumerov and S. Neretina, *Nanotechnology*, 2017, **28**, 282002.
207 D. Kowalski, D. Kim and P. Schmuki, *Nano. Today*, 2013, **8**, 235–264.
208 C. Zhang, R. Huang, Y. Wang, Z. Wu, H. Zhang, Y. Li, W. Wang, C. Huang and L. Li, *ACS Appl. Mater. Interfaces*, 2020, **12**, 1436–1443.
209 M. S. Reis and N. Ma, *Phys. Open*, 2020, **4**, 1–7.
210 A. T. Jones, C. P. Scheller, J. R. Prance, Y. B. Kalyoncu, D. M. Zumbuhl and R. P. Haley, *J. Low Temp. Phys.*, 2020, **201**, 772–802.
211 Y. Tokiwa, S. Bachus, K. Kavita, A. Jesche, A. A. Tsirlin and P. Gegenwart, *Comput. Mater.*, 2021, **2**, 42.